ENGINEERING

Ultrathin thermoresponsive self-folding 3D graphene

Weinan Xu,[1] Zhao Qin,[2] Chun-Teh Chen,[2] Hye Rin Kwag,[1] Qinli Ma,[3] Anjishnu Sarkar,[1] Markus J. Buehler,[2] David H. Gracias[1,4]*

Graphene and other two-dimensional materials have unique physical and chemical properties of broad relevance. It has been suggested that the transformation of these atomically planar materials to three-dimensional (3D) geometries by bending, wrinkling, or folding could significantly alter their properties and lead to novel structures and devices with compact form factors, but strategies to enable this shape change remain limited. We report a benign thermally responsive method to fold and unfold monolayer graphene into predesigned, ordered 3D structures. The methodology involves the surface functionalization of monolayer graphene using ultrathin noncovalently bonded mussel-inspired polydopamine and thermoresponsive poly(*N*-isopropylacrylamide) brushes. The functionalized graphene is micropatterned and self-folds into ordered 3D structures with reversible deformation under a full control by temperature. The structures are characterized using spectroscopy and microscopy, and self-folding is rationalized using a multiscale molecular dynamics model. Our work demonstrates the potential to design and fabricate ordered 3D graphene structures with predictable shape and dynamics. We highlight applicability by encapsulating live cells and creating nonlinear resistor and creased transistor devices.

INTRODUCTION

Two-dimensional (2D) nanomaterials, including graphene, boron nitride, and transition metal dichalcogenides, have been extensively studied due to their promising applications in flexible electronics, energy conversion and storage, plasmonics, and sensing (*1*, *2*). The majority of prior work involves devices in which these 2D materials are in an inherently planar geometry (*3*). However, some applications such as wearable electronics, biological or dispersible sensors, and actuators could benefit from curved and folded architectures that feature small form factors (*4*, *5*). In addition, it has been suggested that the physical and chemical properties of these 2D materials could be strongly affected by the introduction of curvature, folds, and creases (*6*, *7*).

There have been a number of previous reports of folding or wrinkling of graphene, which leverage the atomically thin and extremely low bending stiffness of graphene (*8*). For example, previous studies have shown that suspended graphene sheets can fold under intense mechanical stimulation (*9*) or when curved templates are used during growth (*10*) or transfer (*11*, *12*). Elsewhere, interfacial forces (*13*) and prestretched or thick gradient cross-linked polymer-graphene bilayers have been utilized to induce wrinkling or folding of graphene (*14*, *15*). Although these methods are inspiring, they offer only limited precision and tunability in the three-dimensional (3D) geometries that can be formed or require harsh conditions or significantly thicken the folded graphene due to their reliance on thick substrates or multilayer structures (*16*, *17*).

In contrast, theoretical studies suggest that such folding could be precisely controlled resulting in novel 3D geometries such as flowers, capsules, knots, rings, and boxes (*18*, *19*). These approaches necessitate that folding be carried out with patterned graphene (*20*, *21*). Manual folding of kirigami-patterned graphene has been demonstrated, and shapes such as springs, stretchable electrodes, and hinges have been formed using external mechanical forces (*22*). However, controlled self-folding in response to external environmental stimuli, such as mild temperature compatible with biological systems, has yet to be demonstrated. Such controlled self-folding is extremely difficult to achieve with pristine graphene because graphene by itself is highly chemically inert and does not respond to most external stimuli. Hence, surface functionalization of graphene is necessary, while at the same time, it is also important that the sp^2 hybridization and excellent intrinsic electrical properties of graphene are retained.

Here, we report a strategy to modify the surface of graphene to endow it with thermoresponsive properties and pattern the functionalized graphene into ultrathin self-folding precursors. First, we used polydopamine (PD), a mussel-inspired bioadhesive, to functionalize the surface of graphene in a noncovalent manner (*23*). PD also enables a wide variety of chemical reactions for subsequent functionalization due to its reactive catechol/quinone groups (*24*, *25*), so that responsive polymers, such as poly(*N*-isopropylacrylamide) (PNIPAM) used in this study, can be further grafted to the surface (*26*, *27*). We patterned the functionalized monolayer graphene into a variety of sizes and shapes using photolithography and plasma etching. Then, we released the functionalized graphene patterns from the substrate, and upon heating above the lower critical solution temperature (LCST) of PNIPAM, the 2D precursors self-folded into ordered 3D microstructures induced by the molecular conformational change of the grafted polymer brushes. Note that the functionalized graphene is extremely thin, in the range of 5 to10 nm. In addition, the noncovalent method preserves the intrinsic properties of graphene and its low bending stiffness (*28*). Because the designs of the 2D precursors can be readily controlled using computer-aided design photomasks, we anticipate that this general approach is highly tunable and can be used to fabricate a range of 3D carbon structures of relevance in foldable electronics, biosensing, and molecular robots (*29*); and we highlight some applications.

RESULTS

Surface functionalization of graphene

Graphene is a highly chemically inert material due to the sp^2 hybridization of the carbon atoms on the basal plane (*30*), and thus, covalent functionalization of pristine graphene typically requires highly reactive

[1]Department of Chemical and Biomolecular Engineering, Johns Hopkins University, Baltimore, MD 21218, USA. [2]Department of Civil and Environmental Engineering, Massachusetts Institute of Technology, Cambridge, MA 02139, USA. [3]Department of Physics and Astronomy, Johns Hopkins University, Baltimore, MD 21218, USA. [4]Department of Materials Science and Engineering, Johns Hopkins University, Baltimore, MD 21218, USA.
*Corresponding author. Email: dgracias@jhu.edu

chemicals and harsh conditions (*31*). Moreover, covalent functionalization usually introduces a large number of defects in graphene, which has an adverse effect on its intrinsic electrical properties and stability (*32*). Therefore, in this study, we developed a mild and eco-friendly method to noncovalently functionalize graphene and introduce stimuli-responsive properties.

In the first step, we self-polymerized dopamine on the graphene surface via pH-induced oxidation at room temperature (*33*), which resulted in a very thin layer (~5 nm in the dry state) of PD on the surface of graphene (Fig. 1A). The PD layer makes the surface of monolayer graphene hydrophilic (*34*) and allows further covalent attachment of other molecules and polymers containing functional groups that can react with PD. The strong attachment of PD to the surface of graphene is mostly due to physical interactions, such as π-π stacking and hydrophobic forces (*24*). In the second step, we used the PD thin film as an intermediate active layer to graft the PNIPAM chains. The chemical grafting mechanism is mainly a result of the reaction between the amine end groups of PNIPAM and the functional groups on PD, as discussed in a previous report (*35*).

We investigated the structure of monolayer graphene before and after surface functionalization using Raman spectroscopy, atomic force microscopy (AFM), and X-ray photoelectron spectroscopy (XPS). The Raman spectrum of the pristine monolayer graphene shows the characteristic G and 2D band at 1591 and 2693 cm^{-1}, respectively, and there is also a very weak D band at 1350 cm^{-1}. The intensity ratio I_{2D}/I_G is 2.0, which indicates high-quality monolayer graphene (Fig. 2A) (*36*). To investigate the time dependence of the reactions and tune the thickness of the grafting layers, we varied the polymerization time of PD from 2 to 4 hours (denoted as PD2 and PD4) and that of PNIPAM from 12 to 18 and 24 hours (denoted as PNIPAM12, PNIPAM18, and PNIPAM24). Spectra taken after functionalization at different time points for PD and PNIPAM indicate that the peak intensity and I_{2D}/I_G ratio is largely preserved, suggesting that there is no significant bond breakage in the monolayer graphene during functionalization (fig. S1) (*37*).

The AFM results indicated that the thickness increases from about 0.8 nm for pristine monolayer graphene to 6.0 and 6.9 nm for G-PD2 and G-PD4, respectively (Fig. 2B and fig. S2). The surface of G-PD was relatively uniform, which indicates a strong interaction between PD and the graphene surface. After further grafting of PNIPAM, the thickness of the G-PD-PNIPAM further increased to 8.5, 8.9, and 9.6 nm for grafting reaction times of 12, 18, and 24 hours. In subsequent experiments, unless specifically mentioned, the functionalization of graphene was done with PD grafting time of 2 hours and PNIPAM grafting time of 18 hours, and we refer to these samples as G-PD and G-PD-PNIPAM, respectively.

We characterized the chemical composition of the functionalized graphene using XPS (fig. S3 and table S1). After surface functionalization with PD and PNIPAM, there are significant changes to the C1s (Fig. 2C), N1s (Fig. 2D), and O1s (fig. S4) peaks. For instance, the C1s peak of graphene mainly corresponds to graphite-like sp^2 carbon (284.2 eV) (*38*), whereas that of G-PD can be decomposed to sp^2 C–H on the aromatic rings at 284.0 eV, C–O/C–N species at 285.6 eV, and C=O/C=N species at 287.9 eV (*39*). After PNIPAM grafting, the C1s peak can be decomposed into three peaks, the major one at 285.6 eV for CH_x, another one at 286.7 eV for the C–C=O groups, and the third one at 288.4 eV for the N–C=O groups (*40*). The Raman, AFM, and XPS data together provide strong evidence for the noncovalent surface functionalization of graphene by PD and PNIPAM to a tunable thickness of less than 10 nm.

Fabrication of self-folding microstructures

We observed that after surface functionalization of the graphene, it was endowed with thermoresponsive properties due to the PNIPAM brushes, so that it could behave as an ultrathin shape-changing material. We developed a process to selectively pin down parts of the 2D self-folding precursors while releasing others using a patterned aluminum (Al) sacrificial layer. The parts of the graphene in contact with the underlying SiO_2/Si substrate remain pinned due to strong van der

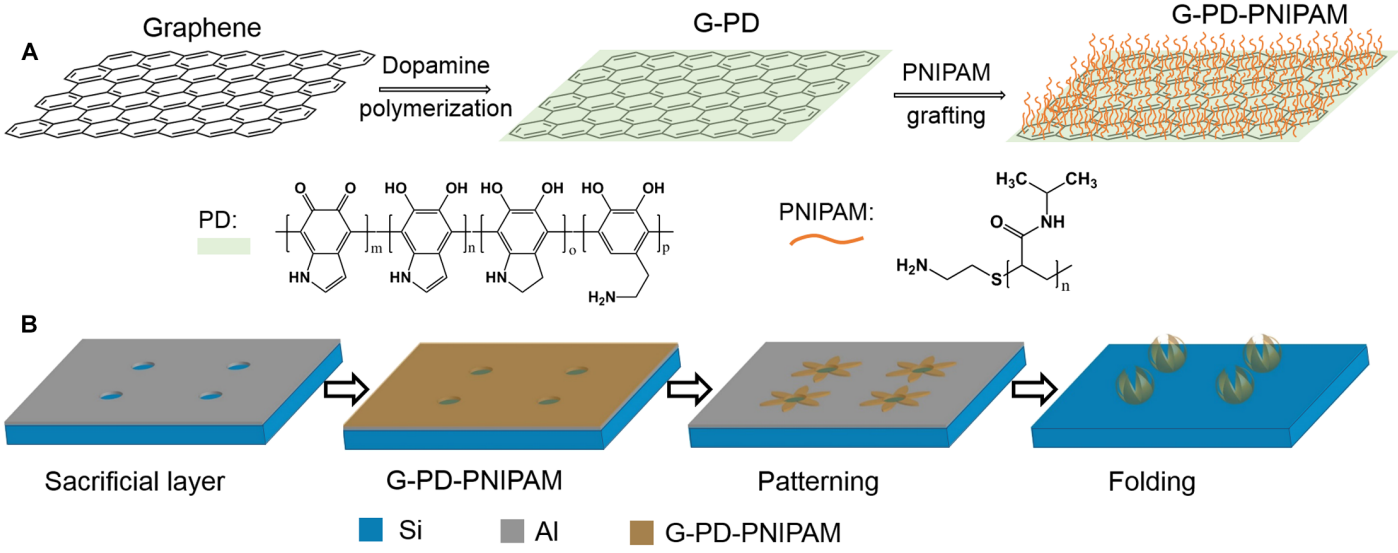

Fig. 1. Surface functionalization and patterning of monolayer graphene. (**A**) Schematic illustration of the surface functionalization process of graphene. In the first step, dopamine was self-polymerized on the surface of graphene to form a thin layer of PD, and then, the amine-terminated PNIPAM chains were grafted on the PD. (**B**) Schematic illustration of the fabrication and folding process of graphene microstructures. First, a patterned Al sacrificial layer was deposited. Then, monolayer graphene was transferred onto the substrate and functionalized using PD and PNIPAM. The functionalized graphene layer was patterned using photolithography and plasma etching. Finally, folding was induced by heating above the LCST of PNIPAM.

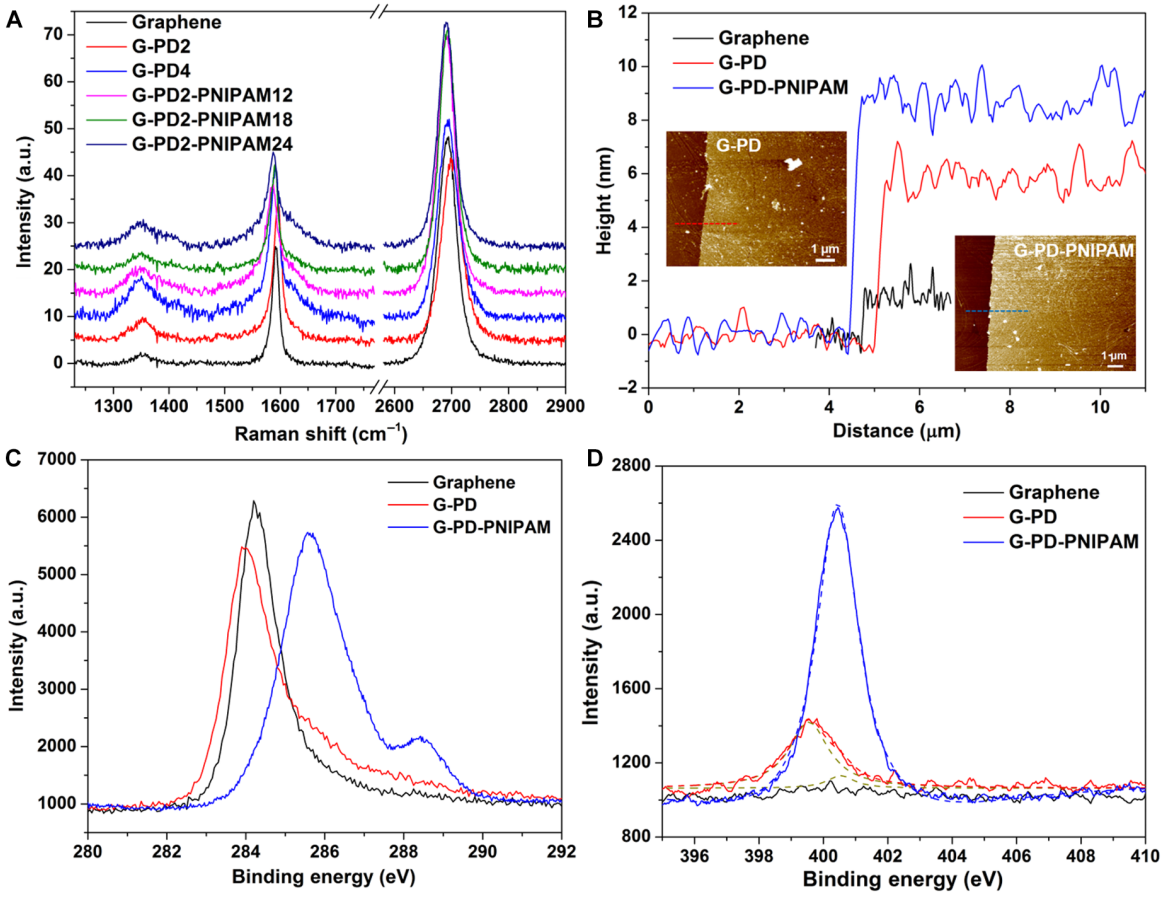

Fig. 2. Characterization of the functionalized graphene. (**A**) Raman spectra of graphene and functionalized graphene with PD and PNIPAM. PDx and PNIPAMx denote self-polymerization times of PD and grafting times of PNIPAM for *x* hours, respectively. a.u., arbitrary unit. (**B**) Representative AFM line scans of the graphene and functionalized graphene measured from the AFM images (insets). (**C** and **D**) XPS spectra (solid line) and peak fitting (dotted line) of graphene and functionalized graphene at the (C) C1s and (D) N1s binding energy regions.

Waals adhesion, whereas the graphene in contact with the Al is released during Al dissolution (Fig. 1B). Selective pinning prevents the folded structures from being washed away, which facilitates characterization, imaging, and device fabrication. If needed, free-floating or untethered self-folded graphene microstructures could also be fabricated using an unpatterned sacrificial layer.

We triggered the self-folding of the microstructures by increasing the temperature to approximately 45°C in aqueous media. The shape of the 2D patterned graphene precursors has a strong influence on their 3D shape after folding. We observed that the flower tends to fold its free petals toward the center and go from an open to a closed state (Fig. 3, A to C), which is useful for the encapsulation of cargo within the ultrathin graphene (*41*). For the dumbbell shape (Fig. 3, D to F), the two circles fold inward; this shape was inspired by the Venus flytrap. We could also self-fold a graphene box using a cruciform precursor (Fig. 3, G to I). In this case, we pinned the center face and released the other five faces. In addition, a rigid SU8 epoxy segment was placed between the two hanging faces to serve as a rigid folding hinge, and its dimensions could be varied without significantly altering the folding (fig. S5).

The scanning electron microscopy (SEM) images of the representative folded structures in the dry state are shown in fig. S6. It can be seen that the functionalized graphene microstructures are stable and uniform and tend to collapse onto the substrate upon drying due to capillary forces. Note that, unlike the previous one-of-a-kind serial folding demonstrations with graphene, this process is highly parallel and structures can be triggered to fold en masse (fig. S7). In addition, using control experiments, we verified that the grafting of thermoresponsive PNIPAM to the surface of graphene is necessary for folding; the pristine graphene and G-PD dumbbell do not show any self-folding behavior at an increased temperature (fig. S8). Furthermore, the thickness of functionalized graphene can be varied in a wide range, down to as low as 5 nm; these ultrathin precursors are still capable of self-folding induced by a temperature increase (fig. S9).

We could achieve selective folding of the graphene microstructures by selective functionalization of different spatial regions with PD and PNIPAM; we observed that only those functionalized regions folded upon heating. The self-folding of the graphene dumbbell with only the right circle functionalized (Fig. 4, A and B) and the graphene flower with the alternating three petals functionalized (Fig. 4, C and D) demonstrate this selectivity. These results indicate a previously unachievable high degree of tunability and control over self-folding monolayer graphene. We observed that the extent of self-folding can be tuned by the temperature for regular-shaped functionalized graphene microstructures and that the extent of folding increased with temperature in the range of 35° to 45°C (fig. S10). The Raman spectrum of the folded functionalized graphene is shown in fig. S11.

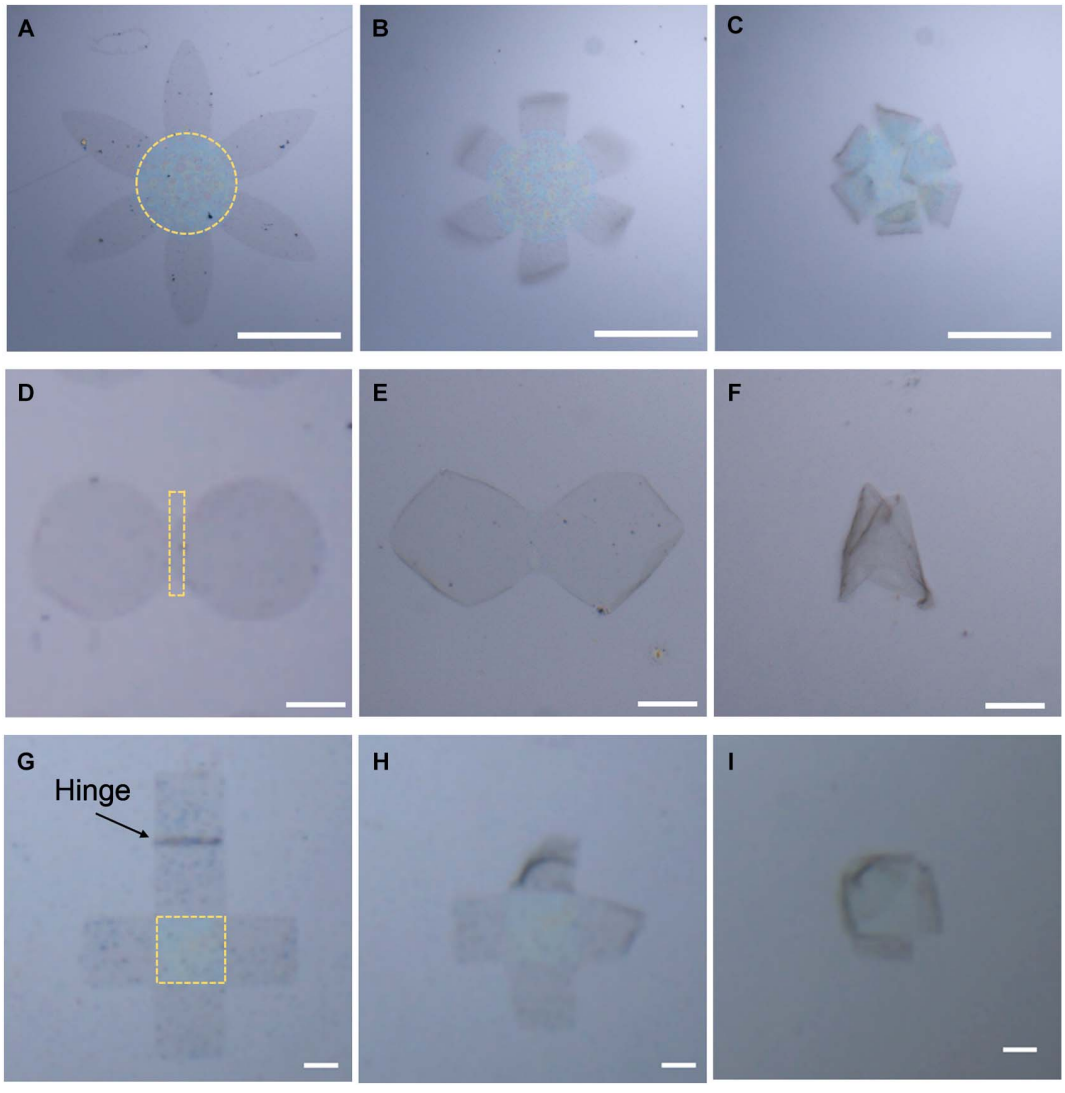

Fig. 3. Temperature-induced self-folding. Optical microscope snapshots of the self-folding of ultrathin graphene microstructures with different geometries: (**A** to **C**) flower, (**D** to **F**) dumbbell, and (**G** to **I**) box. The first column is at room temperature and before folding, the second column is a folding intermediate, and the third column is the folded structure after heating to 45°C. All the optical images were taken in an aqueous environment. Yellow dash lines indicate the pinned down area. Scale bars, 100 μm. The dimension of the rigid SU8 hinge in (G) has a length of 200 μm and a width of 25 μm.

We also achieved reversibility in self-folding by temperature control (Fig. 4E). For example, we could unfold a closing graphene flower by cooling it down from 45° to 25°C, which is consistent with the reversible switching behavior of PNIPAM from collapsed to swollen state at these temperatures. However, note that when the ultrathin graphene petals touched each other during folding, they irreversibly bonded due to the strong van der Waals interactions and were unable to unfold. We found that by adding a rigid polymer layer (SU8) to the petals, we could attenuate the influence of the van der Waals interaction and reduce adhesion between petals, which results in more reversible self-folding but increases the thickness of the precursors (at the rigid panels) to more than 100 nm (Fig. 4F).

One of the highlights of our approach is that the self-folding process utilizes benign thermoresponsive conditions compatible with cell biology. We demonstrate this feature by encapsulating live cells within the self-folding flower. We observed that unlike bare graphene, high densities of cells could be cultured on G-PD-PNIPAM similar to that on a glass substrate, indicating good cell affinity (fig. S12). To encapsulate live cells inside the self-folded graphene microstructures, we first patterned the functionalized graphene into a flower-shaped precursor, and then, the cells were cultured on it. The elevated temperature during cell culture (37°C) induced the folding of the functionalized graphene flowers and encapsulated cells inside the petals (Fig. 4G). We confirmed that the cells are alive after encapsulation within the ultrathin functionalized graphene (Fig. 4H). This result suggests that the self-folding process is biocompatible and can be used to capture biological cargo.

Moreover, by decreasing the size of the functionalized graphene flower to 60 μm, even a single cell can be encapsulated inside (Fig. 4, G and H, insets), which is useful for single cell analysis (*42*). In addition, because of the ultrathin and flexible nature of the functionalized self-folded graphene, it can conform with the surface of the cell, which is important for biosensing applications. For example, we performed Raman characterization of a live cell encapsulated in the functionalized graphene, and the results indicate that the Raman signals from the

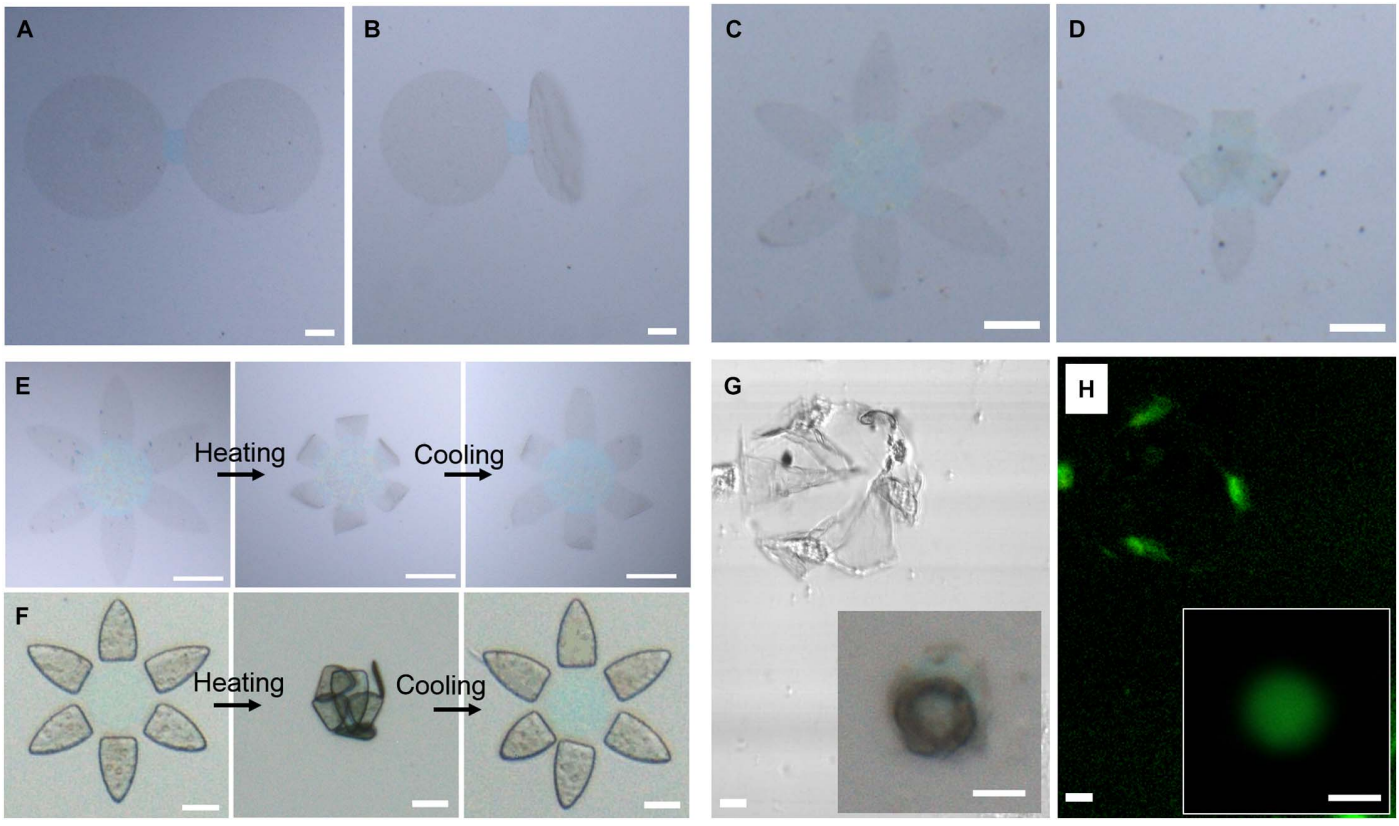

Fig. 4. Selective folding, reversibility, and live cell encapsulation. (**A** to **D**) Selectivity of self-folding in graphene microstructures induced by heating. (A) Optical microscope image of a dumbbell with only its right circle functionalized and (C) a flower with alternating three petals functionalized. (B and D) Optical images of folded structures indicating that only the functionalized regions self-fold on heating. (**E** and **F**) Reversibility of the temperature-induced self-folding. The sequence in (E) shows the folding and unfolding of a functionalized graphene flower, whereas the sequence in (F) shows the folding and unfolding of a flower with rigid SU8 petals, with better stability and reversibility but with increased thickness. (**G** and **H**) Encapsulation of live breast cancer cells within the functionalized graphene flowers. (G) Bright-field and (H) corresponding fluorescence image of encapsulated cells. Cells were stained with a live/dead (calcein AM/ethidium homodimer-1), and green fluorescence indicates viability. Insets in (G) and (H) show the encapsulation of a single breast cancer cell with a 60-μm flower. Scale bars, 50 μm, except for (G) and (H), which are 10 μm.

relevant biological molecules (for example, proteins and phospholipids) in the cell are significantly enhanced (fig. S13).

Multiscale simulations of folding

We developed a mesoscale coarse-grained molecular dynamics (MD) model of the G-PD-PNIPAM structure with its numerical parameters assigned on the basis of the mechanical characterization of different materials learnt from the full atomistic MD simulations. This model was used as an efficient tool to simulate the effect of the thermal stimulus on the structure deformation to gain an in-depth understanding of the folding mechanism and rationalize the self-folded 3D shapes. For a film with a bilayer structure, in which the two layers have different swelling/shrinking properties, it is well known that the strain mismatch will induce the film to bend or form 3D structures (*43*). Such strain mismatch–induced folding has been demonstrated for various materials, such as metals, semiconductors, and polymers (*44*, *45*). However, for ultrathin materials, such as graphene and other 2D materials, such folding has not been achieved or well studied before.

The G-PD-PNIPAM in this work can be simplified as a bilayer material modeled by an elastic network composed of coarse-grained mass beads connected by elastic springs that define both the mechanical stiffness and equilibrium volume of the material (details in Materials and Methods and the Supplementary Materials). The bottom layer consists of a monolayer graphene and thin PD film, which is inert and does not actively swell or shrink due to change in temperature, and thus, the bottom layer is considered as a passive layer only for mechanical stiffness; the top layer consists of PNIPAM brushes, which will shrink when temperature is increased above LCST, and thus, the top layer is considered as an active layer with its equilibrium volume change during the simulation.

We conducted a full atomistic computational study on PNIPAM and PD using MD simulations (details in Materials and Methods) to provide the required mechanical property and structural parameters for the coarse-grained MD model. Figure 5A shows the aggregate structure of PNIPAM brushes (see also fig. S14) at different temperatures: swollen and hydrated at 275 K and shrunken and dehydrated at 325 K. Because of the hydrophobic effect, the total volume of the material at 325 K is only 51% of that at 275 K (fig. S15). Subsequently, tensile tests (see the Supplementary Materials for details) were performed to estimate the Young's modulus of PNIPAM (*46*), and the results show that the Young's moduli are 94 and 243 MPa at 275 and 325 K, respectively (table S2). In addition, the Young's modulus of PD is around 5 GPa according to our previous simulation (*47*, *48*) and experimental results (*49*). Although graphene is extremely stiff, the bending stiffness of the graphene layer is negligible due to its small thickness compared to other layers.

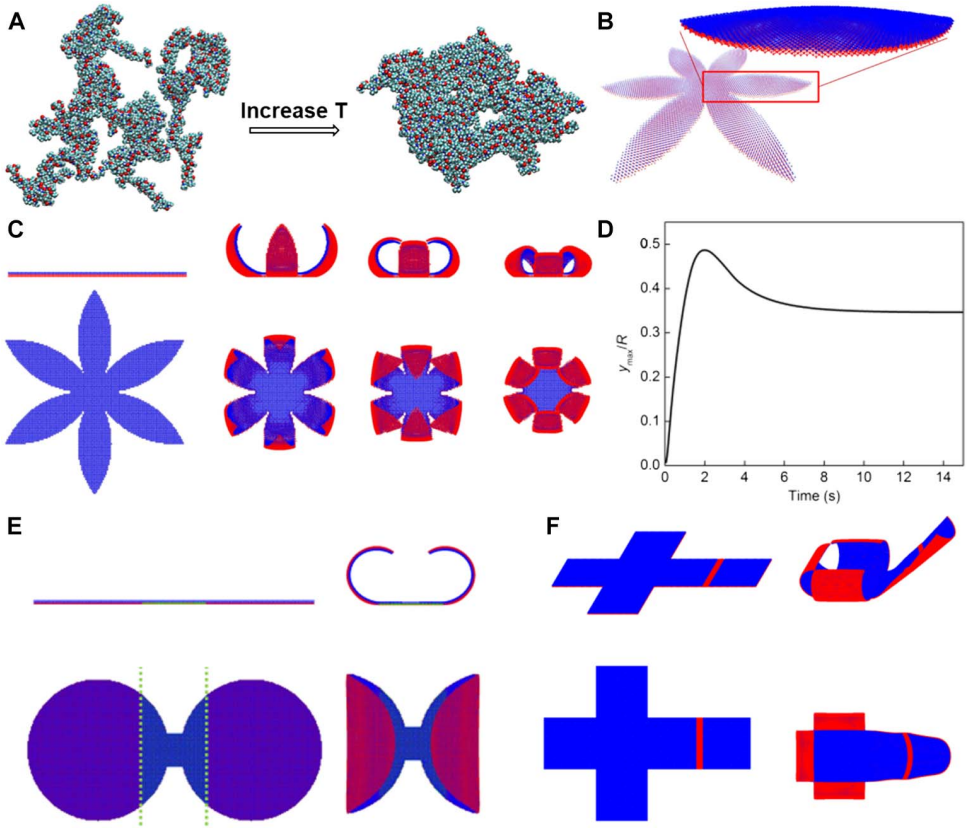

Fig. 5. Multiscale modeling of the temperature-driven self-folding of the functionalized graphene. (**A**) Top view of the aggregation of an array of PNIPAM brushes with increasing temperatures in full atomistic MD simulations (cyan, C; red, O; blue, N; white, H). (**B**) A representative mesoscale coarse-grained model of the flower-shaped functionalized graphene. (**C**) Simulation snapshots of the coarse-grained model during the folding process of the functionalized graphene flower. The first row is the side view, and the bottom row is the top view. (**D**) Plot of the height versus the overall initial radius of the flower pattern over time. (**E** and **F**) Flat and folded states of the dumbbell and box shaped graphene from simulation. The top row is the side/tilted view, and the bottom row is the top view. The coarse-grained structure is colored according to different materials: blue for the PNIPAM layer and red for the PD-graphene layer. A certain region of the bottom layer of coarse-grained beads is fixed by adapting the same boundary condition as in the experiments.

We parametrized the elastic springs in the coarse-grained model according to the full atomistic simulations (see Materials and Methods and the Supplementary Materials for details), and the overall geometry of the model was of three sets of different shapes: flower, dumbbell, and box. Note that this model enables us to define the equilibrium volume and material stiffness as an explicit function of the temperature and, thus, allows us to efficiently simulate its temperature response. The deformations of the multilayered G-PD-PNIPAM structures of these shapes are summarized in Fig. 5. We found that the folding is induced by shrinking of the PNIPAM layer to 51% of its original volume, when the temperature increases from 275 to 325 K. The entire folding process of the flower shape can be closely monitored (Fig. 5C), and the entire deformation process can be traced by the overall height of the folded structure, showing that the folded structure can first reach a peak height and then coil to reach equilibrium after a certain amount of time (Fig. 5D). The simulation and experiment results are consistent. For instance, for the self-folding graphene flower, the average lateral size and height in the folded state measured by confocal microscopy were found to be 131 (±14) and 58 (±17) μm (Fig. 3C), and those values are 125 and 52 μm (Fig. 5C) in the simulation. A qualitative comparison was conducted between the simulation and experimental results for self-folding structures with different sizes (fig. S16).

We also theoretically investigated the effect of the modulus ratio between the top and bottom layers on their folding behavior. We observed that similar fully folded geometries could be achieved by a range of stiffness ratio of the two layers (fig. S17), suggesting the consistent geometry of the folded structure. Similarly, the modeling of the folding process of the dumbbell shape, which folds toward the center, is shown in Fig. 5E. Figure 5F shows the folding of the patterned functionalized graphene into a box shape; it is worth mentioning that in the simulation, the box is not fully closed, but in the experiment, because of the small perturbation of water flow at elevated temperature, the ultrathin faces can fold more toward the center, which results in a more closed box. We have also used this material model to design other material systems with different deformation ratio and material stiffness. It was suggested by these simulations that we can also change the fixed boundary condition and distribution pattern of the PNIPAM layer to create different folded geometries.

Nonlinear resistors and creased transistors

Apart from its applicability as ultrathin encapsulating devices, self-folding can also be used as a means to tune the electrical properties of graphene. We measured the conductivity of the functionalized

graphene microstructure using the four-point probe method, and the gold electrodes were placed directly on graphene before it was functionalized with PD and PNIPAM. The *I-V* curve for G-PD-PNIPAM in the flat state shows a linear behavior with a sheet resistance of 430 ohm/sq, which is approximately the same as that measured on pristine monolayer graphene (fig. S18) and similar to that reported previously in the literature (*50*). This result further confirms that the functionalization is noncovalent in nature and does not compromise the excellent conductivity of graphene.

In contrast, the electrical properties change dramatically after folding and crease formation. We measured the *I-V* characteristics of self-folding functionalized graphene dumbbells (Fig. 6A). After self-folding and drying, the right circle folds on top of the left circle forming a crease, the diameter of which was measured by AFM to be around 18 nm (fig. S19). Note that we insulated the two graphene layers in the flat region with a 100-nm-thick SU8 layer to eliminate interlayer tunneling. After folding, the *I-V* curve becomes nonlinear, and there is a significant increase of resistance by approximately threefold from 2.08 kilohms to a voltage-dependent resistance ranging from 5.47 to 7.67 kilohms (Fig. 6, B and C), with the maximum resistance at around 0 V. We attribute this increase in resistance to the introduction of a folding crease region. Previously, it has been reported that folded graphene nanochannel structures also showed nonlinear *I-V* curves with increased resistance (*51*, *52*), which is consistent with our observations. In our approach, the magnitude of resistance increase can also be tuned by changing the dimension of the folding crease (fig. S18).

We also fabricated back-gated graphene field-effect transistors (FETs) to further study the effect of folding crease on the electronic properties of graphene (Fig. 6D). All the measurements were done at room temperature under ambient conditions. Before folding, the transfer curve (Fig. 6E) shows that the drain current (I_d) gradually decreases with increasing gate voltage (V_g), and the Dirac point is approximately +90 V, which indicates that the graphene is heavily p-doped. This behavior is also observed in pristine graphene FETs (fig. S20), and a possible reason for this shift in the Dirac point is the adsorption of water molecules from air and the polymer residue from the transfer process (*53*).

After folding, the transfer curve shows that in addition to the Dirac point at around +90 V, there is a new minimum observed at around −30 V. A similar feature has been observed in a previous report (*54*), and it is believed that the new minima are related to the folding crease, which induces strong gauge fields and alters the charge carrier densities. In addition, the I_d is almost one order of magnitude lower than that of the flat state at the same drain voltage, which indicates a significant increase in the resistance of the graphene channel due to the folding crease (Fig. 6F and fig. S20). We rationalize this observation by noting that the folding crease behaves as a tunnel barrier for the current flow; the exact mechanism for the formation of these barriers in folded graphene or nanoribbons is still in debate. Plausible explanations have been previously attributed to the formation of an energy band gap due to the confinement (*55*) and the formation of a series of quantum dots induced by a disorder potential (*56*).

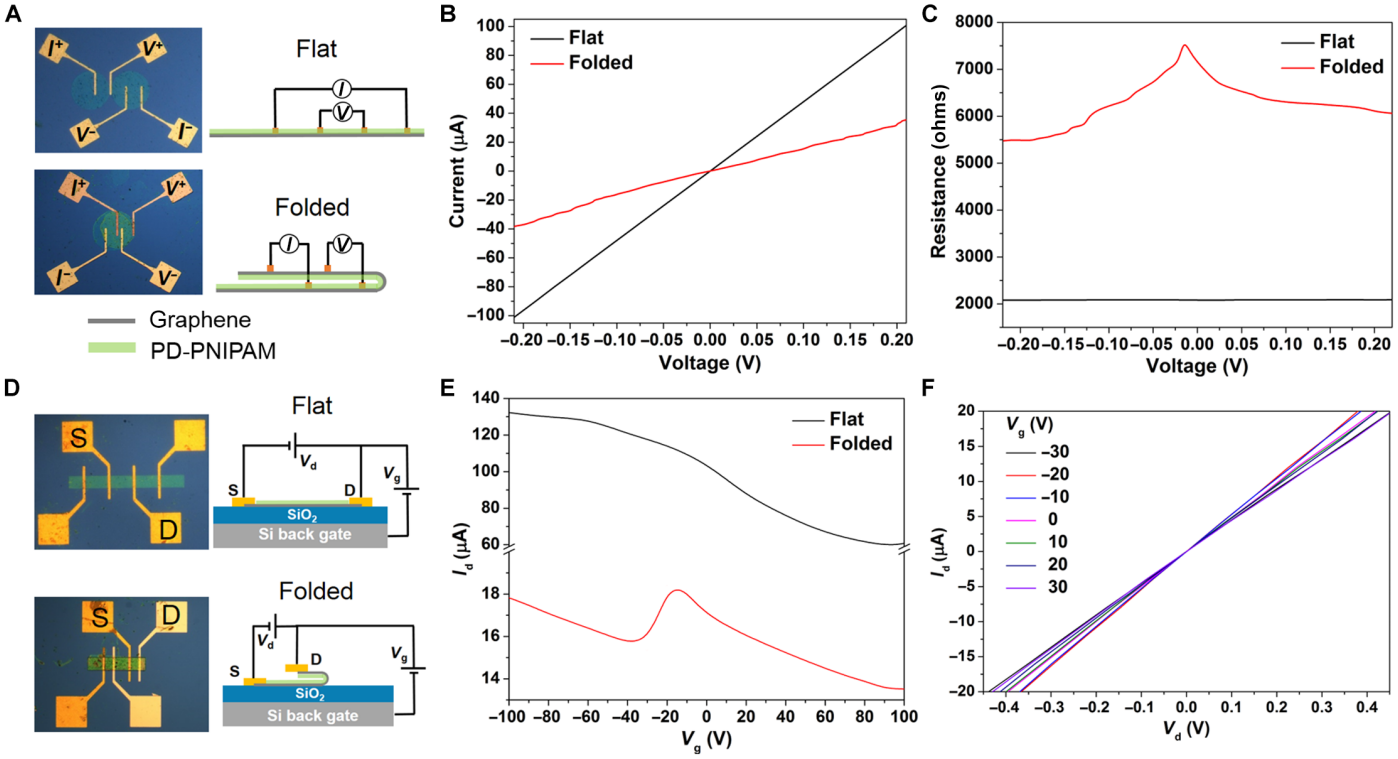

Fig. 6. Graphene-based nonlinear resistors and creased transistor devices. (**A**) Optical images and circuit diagrams of the measured resistor devices in the flat (top) and folded (bottom) states. (**B**) Representative *I-V* curves of a graphene dumbbell before and after folding. (**C**) *R-V* curves of the same samples as shown in (B). (**D**) Optical images and circuit diagrams of the measured graphene FETs in the flat (top) and folded (bottom) states. (**E**) The transfer curves of the functionalized graphene FET as a function of back-gate voltage in the flat (black line) and folded (red line) states. (**F**) Output curves of the functionalized graphene FET in the folded state as a function of drain voltage with varying gate voltages.

DISCUSSION

Graphene has been extensively studied in its planar form, and the ability to manipulate graphene and fold the atomically thin sheet into 3D shapes represents a new direction with the possibility to create new types of devices. However, because graphene is chemically inert, it is very challenging to achieve this transformation without altering the intrinsic properties of graphene. Here, we showed how this can be done using a noncovalent functionalization method. Our method has several unique advantages compared with previous reports: First, the noncovalent nature of PD surface functionalization does not compromise the electrical property of graphene; second, the polymer layer is ultrathin, and its thickness can be accurately controlled by tuning the PD polymerization time and polymer brush length; and third, the functionalization is confined within one side of the monolayer graphene surface and can also be performed on selective regions of graphene when combined with patterning techniques. Hence, the process is highly tunable, and a variety of folding shapes can be formed. Finally, this process is benign and does not require harsh processing conditions and is compatible with cell biology and physiological conditions.

As highlighted, we envision a number of applications. First, because of the versatility of the surface functionalization and patterning techniques, a variety of origami and kirigami shape-changing structures could be formed. In addition, the temperature responsiveness of PNIPAM is reversible and has been widely utilized to form a range of actuators, so it is anticipated that our approach could extend these to graphene hybrids. Because of the compatibility with living systems, this approach could be used to encapsulate and deliver cells or other biologics. Moreover, because of low bending rigidity, we believe that the graphene can be conformably coated on the surface of 3D objects with intimate contact, which is very important for ultrasensitive detection, biosensing, and drug delivery (*57*). Finally, programmed crease formation driven by self-folding can be used to design novel electrical and field effect devices where the properties of graphene can be tuned on the basis of folding geometries.

MATERIALS AND METHODS

Surface functionalization of graphene

Monolayer graphene on the patterned substrate was immersed in a dilute aqueous solution of dopamine (2.0 mg/ml) (Sigma-Aldrich), buffered to a typical marine environment pH of 8.5 (10 mM tris-HCl), for 2 or 4 hours. A thin layer of PD formed on the graphene surface via self-polymerization. The coated surface was washed thoroughly with deionized water and dried with N_2 gas.

The PD-coated graphene was then immersed into a solution of amine-terminated PNIPAM (2.0 mg/ml) (M_n, 5500; Sigma-Aldrich) dissolved in 10 mM tris-HCl buffer (pH 8.5). The grafting reaction was carried out at 60°C for 3 hours and then cooled down to room temperature and further kept for 12, 18, or 24 hours. The functionalized graphene was thoroughly washed with deionized water and dried with N_2 gas.

Characterization of the functionalized graphene

Raman measurements were done using a Jobin-Yvon T64000 triple monochromator spectrometer with an Olympus microscope. The excitation line was the 514.5-nm line of a Spectra-Physics Ar-Kr laser. XPS data were acquired with a PHI 5400 XPS using Mg Kα X-rays (energy = 1253.6 eV). The peaks in the high-resolution scan were fitted with Shirley backgrounds and a Gaussian-Lorentzian mixed function. AFM was performed in tapping mode with ~300 kHz Si cantilevers on a Bruker AFM (Dimension FastScan). The scan rate was set at 0.5 Hz, and the sampling was at least 512 samples per line by 512 lines.

Fabrication of self-folding graphene microstructures

The functionalized graphene was patterned into various shapes, including flower, dumbbell, and box, by photolithography, and the graphene in unwanted areas was removed using an oxygen plasma [radio frequency (RF) power, 60; time, 30 s] (PE-100; Plasma Etch Inc.). The functionalized graphene was released from the substrate by dissolving the underlying Al layer with dilute NaOH (5 mM). The solution also contained 3 mM sodium dodecyl sulfate surfactant to reduce the adhesion of graphene to the surface and prevent the graphene from permanently sticking to itself. A previous study showed that the presence of surfactant molecules does not measurably affect the mechanical and electrical properties of graphene (*22*). Folding of the functionalized graphene was induced by increasing the temperature after dissolving the Al sacrificial layer. The solution was heated to 45°C using a hot plate, and the temperature was monitored during the entire process with a thermometer.

Characterization of folded graphene microstructures

Optical microscope images were taken in aqueous condition using a Nikon AZ100 microscope equipped with a mercury lamp (Nikon C-HGFI). SEM images were taken with the FEI Quanta 200 microscope. The resistance of the graphene microstructures was measured using the conventional four-point probe method, where a constant current was generated from the Keithley 220 current source, and the voltage was measured using a Keithley 2182A Nanovoltmeter. We fabricated back-gated graphene transistors on a Si/SiO_2 substrate (p^+-doped, ρ ~ 0.001 to 0.005 ohm cm; Silicon Materials Inc.). We evaporated 5 nm of Cr (adhesion layer) and 50 nm of Au for source and drain contacts to the graphene. The transport channel defined by the two electrodes deposited on graphene was 125 μm wide and 230 μm long. All the measurements were performed at room temperature.

Full atomistic modeling and equilibration

To obtain the required coefficients for our coarse-grained MD model, full atomistic MD simulations of PNIPAM were performed using the Large-scale Atomic/Molecular Massively Parallel Simulator (LAMMPS) (*58*). The full atomistic PNIPAM model consists of 36 PNIPAM chains with a chain length of 20-mer. In the initial configuration (fig. S14), the longitude direction of each PNIPAM chain is faced to the *x*-direction of the simulation box, and the PNIPAM chains are separated by a distance of 30 Å in both the *y* and *z* directions. The simulations were conducted in the presence of explicit water, and the mass of the PNIPAM chains was around 10% of the mass of the water molecules in the PNIPAM-water system. In the simulation, the CHARMM (Chemistry at Harvard Macromolecular Mechanics) General Force Field (CGenFF) was adopted (*59*), and the CGenFF code was used to create the parameter file (*60*). Periodic boundary conditions were applied in all three directions. After energy minimization, which was performed with the conjugate gradient algorithm, the PNIPAM-water system was equilibrated with the isothermal-isobaric (NPT) ensemble at a temperature of 275 K and pressure of 1.013 bar in the *y* and *z* directions for 20 ns. To study the temperature effects on the structural and mechanical

properties of PNIPAM, another PNIPAM-water system was equilibrated with the NPT ensemble at a temperature of 325 K and pressure of 1.013 bar in the y and z directions for 20 ns. More details can be found in the Supplementary Materials.

Coarse-grained modeling and equilibration

The face-centered cubic lattice was used to model the location of the mass beads (which locate at corners and face centers), and an elastic spring was used to model the interaction between the nearest neighboring beads. The effect of the temperature on the PNIPAM brush layer was implicitly simulated by tuning the equilibrium length constant of the lattice structure as

$$a(t) = a_{\text{end}} + (a_0 - a_{\text{end}}) \exp\left(-\frac{t}{t_0}\right)$$

In the above equation, $a_0 = 4$ μm is the initial lattice length at low temperature, $a_{\text{end}} = 0.71\ a_0$ is the equilibrium length constant at high temperature, which reflects the 49% in-plane volume change for one length dimension, and t_0 is the time constant used in the simulations to reflect how quick the PNIPAM responds to the temperature change. More details can be found in the Supplementary Materials.

SUPPLEMENTARY MATERIALS

Supplementary material for this article is available at http://advances.sciencemag.org/cgi/content/full/3/10/e1701084/DC1

Additional experimental details
Raman spectra of the functionalized graphene
AFM characterization of the functionalized graphene
XPS characterization of functionalized graphene
Optical and SEM imaging of the self-folding graphene structures
Raman spectra of folded graphene
Cell encapsulation and Raman analysis
Full atomistic modeling of the folding behaviors
Electrical properties of folded graphene structures
fig. S1. Raman spectra of PD with different thickness (self-polymerization for 2 and 4 hours) on the Si substrate.
fig. S2. Surface morphology of graphene and functionalized graphene.
fig. S3. Chemical composition of functionalized graphene studied by XPS.
fig. S4. High-resolution O1s XPS spectra and peak fitting (dotted lines) of graphene, G-PD, and G-PD-PNIPAM.
fig. S5. Effect of the rigid hinge on the self-folding of functionalized graphene box.
fig. S6. Characterization of the self-folding graphene microstructures using SEM.
fig. S7. Highly parallel self-folding of ultrathin 3D graphene microstructures.
fig. S8. Control experiments of self-folding on pristine graphene and G-PD.
fig. S9. Self-folding of functionalized graphene with 5 nm thickness.
fig. S10. The folding process of half-functionalized graphene dumbbell with increasing temperature.
fig. S11. Raman spectra of a graphene flower in the flat and folded regions.
fig. S12. Cell viability with the live/dead assay.
fig. S13. Single cell encapsulation and Raman study.
fig. S14. Initial configuration of the PNIPAM-water system in the MD model.
fig. S15. Top view of the aggregation behavior of an array of (36 chains in total) PNIPAM brushes at different temperatures in MD simulations.
fig. S16. Comparison between the coarse-grained MD model and the experiment results for a functionalized graphene flower with different size.
fig. S17. The effect of mechanical properties of the two layers on self-folding.
fig. S18. Electrical measurements on pristine graphene and functionalized graphene dumbbell.
fig. S19. Dimension of the folding crease measured by AFM.
fig. S20. Output and transfer curves of the pristine and functionalized graphene FET.
table S1. XPS data analysis of graphene, G-PD, and G-PD-PNIPAM at the C1s, N1s, and O1s peaks.
table S2. Tensile test results of PNIPAM from the MD simulations.

REFERENCES AND NOTES

1. A. Gupta, T. Sakthivel, S. Seal, Recent development in 2D materials beyond graphene. *Prog. Mater Sci.* **73**, 44–126 (2015).
2. V. Singh, D. Joung, L. Zhai, S. Das, S. I. Khondaker, S. Seal, Graphene based materials: Past, present and future. *Prog. Mater Sci.* **56**, 1178–1271 (2011).
3. F. Schwierz, Graphene transistors. *Nat. Nanotechnol.* **5**, 487–496 (2010).
4. J. A. Rogers, T. Someya, Y. Huang, Materials and mechanics for stretchable electronics. *Science* **327**, 1603–1607 (2010).
5. Y. Chen, F. Guo, A. Jachak, S.-P. Kim, D. Datta, J. Liu, I. Kulaots, C. Vaslet, H. D. Jang, J. Huang, V. B. Shenoy, R. H. Hurt, Aerosol synthesis of cargo-filled graphene nanosacks. *Nano Lett.* **12**, 1996–2002 (2012).
6. S. Deng, V. Berry, Wrinkled, rippled and crumpled graphene: An overview of formation mechanism, electronic properties, and applications. *Mater. Today* **19**, 197–212 (2016).
7. W. Zhu, T. Low, V. Perebeinos, A. A. Bol, Y. Zhu, H. Yan, J. Tersoff, P. Avouris, Structure and electronic transport in graphene wrinkles. *Nano Lett.* **12**, 3431–3436 (2012).
8. C. N. Berger, M. Dirschka, A. Vijayaraghavan, Ultra-thin graphene–polymer heterostructure membranes. *Nanoscale* **8**, 17928–17939 (2016).
9. J. Zhang, J. Xiao, X. Meng, C. Monroe, Y. Huang, J.-M. Zuo, Free folding of suspended graphene sheets by random mechanical stimulation. *Phys. Rev. Lett.* **104**, 166805 (2010).
10. K. Kim, Z. Lee, B. D. Malone, K. T. Chan, B. Alemán, W. Regan, W. Gannett, M. F. Crommie, M. L. Cohen, A. Zettl, Multiply folded graphene. *Phys. Rev. B* **83**, 245433 (2011).
11. J. Zang, S. Ryu, N. Pugno, Q. Wang, Q. Tu, M. J. Buehler, X. Zhao, Multifunctionality and control of the crumpling and unfolding of large-area graphene. *Nat. Mater.* **12**, 321–325 (2013).
12. W.-K. Lee, J. Kang, K.-S. Chen, C. J. Engel, W.-B. Jung, D. Rhee, M. C. Hersam, T. W. Odom, Multiscale, hierarchical patterning of graphene by conformal wrinkling. *Nano Lett.* **16**, 7121–7127 (2016).
13. B. Wang, M. Huang, N. Y. Kim, B. V. Cunning, Y. Huang, D. Qu, X. Chen, S. Jin, M. Biswal, X. Zhang, S. H. Lee, H. Lim, W. J. Yoo, Z. Lee, R. S. Ruoff, Controlled folding of single crystal graphene. *Nano Lett.* **17**, 1467–1473 (2017).
14. D. Joung, A. Nemilentsau, K. Agarwal, C. Dai, C. Liu, Q. Su, J. Li, T. Low, S. J. Koester, J.-H. Cho, Self-assembled three-dimensional graphene-based polyhedrons inducing volumetric light confinement. *Nano Lett.* **17**, 1987–1994 (2017).
15. T. Deng, C. Yoon, Q. Jin, M. Li, Z. Liu, D. H. Gracias, Self-folding graphene-polymer bilayers. *Appl. Phys. Lett.* **106**, 203108 (2015).
16. J. Rogers, Y. Huang, O. G. Schmidt, D. H. Gracias, Origami MEMS and NEMS. *MRS Bull.* **41**, 123–129 (2016).
17. N. Patra, Y. Song, P. Král, Self-assembly of graphene nanostructures on nanotubes. *ACS Nano* **5**, 1798–1804 (2011).
18. N. Patra, B. Wang, P. Král, Nanodroplet activated and guided folding of graphene nanostructures. *Nano Lett.* **9**, 3766–3771 (2009).
19. S. Zhu, T. Li, Hydrogenation-assisted graphene origami and its application in programmable molecular mass uptake, storage, and release. *ACS Nano* **8**, 2864–2872 (2014).
20. D. Akinwande, C. J. Brennan, J. S. Bunch, P. Egberts, J. R. Felts, H. Gao, R. Huang, J.-S. Kim, T. Li, Y. Li, K. M. Liechti, N. Lu, H. S. Park, E. J. Reed, P. Wang, B. I. Yakobson, T. Zhang, Y.-Z. Zhang, Y. Zhou, Y. Zhu, A review on mechanics and mechanical properties of 2D materials—Graphene and beyond. *Extreme Mech. Lett.* **13**, 42–77 (2017).
21. S. Zhu, Y. Huang, T. Li,. Extremely compliant and highly stretchable patterned graphene. *Appl. Phys. Lett.* **104**, 173103 (2014).
22. M. K. Blees, A. W. Barnard, P. A. Rose, S. P. Roberts, K. L. McGill, P. Y. Huang, A. R. Ruyack, J. W. Kevek, B. Kobrin, D. A. Muller, P. L. McEuen, Graphene kirigami. *Nature* **524**, 204–207 (2015).
23. H. Lee, S. M. Dellatore, W. M. Miller, P. B. Messersmith, Mussel-inspired surface chemistry for multifunctional coatings. *Science* **318**, 426–430 (2007).
24. B. H. Kim, D. H. Lee, J. Y. Kim, D. O. Shin, H. Y. Jeong, S. Hong, J. M. Yun, C. M. Koo, H. Lee, S. O. Kim, Mussel-inspired block copolymer lithography for low surface energy materials of teflon, graphene, and gold. *Adv. Mater.* **23**, 5618–5622 (2011).
25. M. d'Ischia, A. Napolitano, V. Ball, C. T. Chen, M. J. Buehler, Polydopamine and eumelanin: From structure–property relationships to a unified tailoring strategy. *Acc. Chem. Res.* **47**, 3541–3550 (2014).
26. C.-T. Chen, F. J. Martin-Martinez, G. S. Jung, M. J. Buehler, Polydopamine and eumelanin molecular structures investigated with ab initio calculations. *Chem. Sci.* **8**, 1631–1641 (2017).
27. W. Xu, P. A. Ledin, Z. Iatridi, C. Tsitsilianis, V. V. Tsukruk, Multiresponsive star-graft quarterpolymer monolayers. *Macromolecules* **48**, 3344–3353 (2015).
28. R. Xiong, K. Hu, A. M. Grant, R. Ma, W. Xu, C. Lu, X. Zhang, V. V. Tsukruk, Ultrarobust transparent cellulose nanocrystal-graphene membranes with high electrical conductivity. *Adv. Mater.* **28**, 1501–1509 (2016).
29. J. Mu, C. Hou, H. Wang, Y. Li, Q. Zhang, M. Zhu, Origami-inspired active graphene-based paper for programmable instant self-folding walking devices. *Sci. Adv.* **1**, e1500533 (2015).

30. I. Choi, D. D. Kulkarni, W. Xu, C. Tsitsilianis, V. V. Tsukruk, Star polymer unimicelles on graphene oxide flakes. *Langmuir* **29**, 9761–9769 (2013).
31. J. Park, M. Yan, Covalent functionalization of graphene with reactive intermediates. *Acc. Chem. Res.* **46**, 181–189 (2013).
32. V. Georgakilas, J. N. Tiwari, K. C. Kemp, J. A. Perman, A. B. Bourlinos, K. S. Kim, R. Zboril, Noncovalent functionalization of graphene and graphene oxide for energy materials, biosensing, catalytic, and biomedical applications. *Chem. Rev.* **116**, 5464–5519 (2016).
33. H. Ren, D. D. Kulkarni, R. Kodiyath, W. Xu, I. Choi, V. V. Tsukruk, Competitive adsorption of dopamine and rhodamine 6G on the surface of graphene oxide. *ACS Appl. Mater. Interfaces* **6**, 2459–2470 (2014).
34. S. Park, J. M. Yun, U. N. Maiti, H.-S. Moon, H. M. Jin, S. O. Kim, Device-oriented graphene nanopatterning by mussel-inspired directed block copolymer self-assembly. *Nanotechnology* **25**, 014008 (2013).
35. B. P. Tripathi, N. C. Dubey, F. Simon, M. Stamm, Thermo responsive ultrafiltration membranes of grafted poly (*N*-isopropyl acrylamide) *via* polydopamine. *RSC Adv.* **4**, 34073–34083 (2014).
36. A. C. Ferrari, J. C. Meyer, V. Scardaci, C. Casiraghi, M. Lazzeri, F. Mauri, S. Piscanec, D. Jiang, K. S. Novoselov, S. Roth, A. K. Geim, Raman spectrum of graphene and graphene layers. *Phys. Rev. Lett.* **97**, 187401 (2006).
37. B. Fei, B. Qian, Z. Yang, R. Wang, W. C. Liu, C. L. Mak, J. H. Xin, Coating carbon nanotubes by spontaneous oxidative polymerization of dopamine. *Carbon* **46**, 1795–1797 (2008).
38. J. Park, W. C. Mitchel, S. Elhamri, L. Grazulis, J. Hoelscher, K. Mahalingam, C. Hwang, S.-K. Mo, J. Lee, Observation of the intrinsic bandgap behaviour in as-grown epitaxial twisted graphene. *Nat. Commun.* **6**, 5677 (2015).
39. R. A. Zangmeister, T. A. Morris, M. J. Tarlov, Characterization of polydopamine thin films deposited at short times by autoxidation of dopamine. *Langmuir* **29**, 8619–8628 (2013).
40. Z.-L. Gong, D.-Y. Tang, Y.-D. Guo, The fabrication and self-flocculation effect of hybrid TiO_2 nanoparticles grafted with poly(*N*-isopropylacrylamide) at ambient temperature via surface-initiated atom transfer radical polymerization. *J. Mater. Chem.* **22**, 16872–16879 (2012).
41. J. M. Yuk, J. Park, P. Ercius, K. Kim, D. J. Hellebusch, M. F. Crommie, J. Y. Lee, A. Zettl, A. P. Alivisatos, High-resolution EM of colloidal nanocrystal growth using graphene liquid cells. *Science* **336**, 61–64 (2012).
42. Q. Jin, M. Li, B. Polat, S. K. Paidi, A. Dai, A. Zhang, J. V. Pagaduan, I. Barman, D. H. Gracias, Mechanical trap surface-enhanced Raman spectroscopy for three-dimensional surface molecular imaging of single live cells. *Angew. Chem. Int. Ed.* **56**, 3822–3826 (2017).
43. S. Xu, Z. Yan, K.-I. Jang, W. Huang, H. Fu, J. Kim, Z. Wei, M. Flavin, J. McCracken, R. Wang, A. Badea, Y. Liu, D. Xiao, G. Zhou, J. Lee, H. U. Chung, H. Cheng, W. Ren, A. Banks, X. Li, U. Paik, R. G. Nuzzo, Y. Huang, Y. Zhang, J. A. Rogers Assembly of micro/nanomaterials into complex, three-dimensional architectures by compressive buckling. *Science* **347**, 154–159 (2015).
44. V. B. Shenoy, D. H. Gracias, Self-folding thin-film materials: From nanopolyhedra to graphene origami. *MRS Bull.* **37**, 847–854 (2012).
45. Z. L. Wu, M. Moshe, J. Greener, H. Therien-Aubin, Z. Nie, E. Sharon, E. Kumacheva, Three-dimensional shape transformations of hydrogel sheets induced by small-scale modulation of internal stresses. *Nat. Commun.* **4**, 1586 (2013).
46. C.-T. Chen, S. Ghosh, C. M. Reddy, M. J. Buehler, Molecular mechanics of elastic and bendable caffeine co-crystals. *Phys. Chem. Chem. Phys.* **16**, 13165–13171 (2014).
47. C.-T. Chen, V. Ball, J. J. de Almeida Gracio, M. K. Singh, V. Toniazzo, D. Ruch, M. J. Buehler, Self-assembly of tetramers of 5,6-dihydroxyindole explains the primary physical properties of eumelanin: Experiment, simulation, and design. *ACS Nano* **7**, 1524–1532 (2013).
48. C.-T. Chen, C. Chuang, J. Cao, V. Ball, D. Ruch, M. J. Buehler, Excitonic effects from geometric order and disorder explain broadband optical absorption in eumelanin. *Nat. Commun.* **5**, 3859 (2014).
49. S. Lin, C.-T. Chen, I. Bdikin, V. Ball, J. Grácio, M. J. Buehler, Tuning heterogeneous poly(dopamine) structures and mechanics: In silico covalent cross-linking and thin film nanoindentation. *Soft Matter* **10**, 457–464 (2014).
50. K. S. Kim, Y. Zhao, H. Jang, S. Y. Lee, J. M. Kim, K. S. Kim, J.-H. Ahn; P. Kim, J.-Y. Choi, B. H. Hong, Large-scale pattern growth of graphene films for stretchable transparent electrodes. *Nature* **457**, 706–710 (2009).
51. I. Silvestre, A. W. Barnard, S. P. Roberts, P. L. McEuen, R. G. Lacerda, Folded graphene nanochannels via pulsed patterning of graphene. *Appl. Phys. Lett.* **106**, 153105 (2015).
52. S.-F. Shi, X. Xu, D. C. Ralph, P. L. McEuen, Plasmon resonance in individual nanogap electrodes studied using graphene nanoconstrictions as photodetectors. *Nano Lett.* **11**, 1814–1818 (2011).
53. S. Chen, W. Cai, D. Chen, Y. Ren, X. Li, Y. Zhu, J. Kang, R. S. Ruoff, Adsorption/desorption and electrically controlled flipping of ammonia molecules on graphene. *New J. Phys.* **12**, 125011 (2010).
54. H. Schmidt, J. C. Rode, D. Smirnov, R. J. Haug, Superlattice structures in twisted bilayers of folded graphene. *Nat. Commun.* **5**, 5742 (2014).
55. X. Li, X. Wang, L. Zhang, S. Lee, H. Dai, Chemically derived, ultrasmooth graphene nanoribbon semiconductors. *Science* **319**, 1229–1232 (2008).
56. B. Özyilmaz, P. Jarillo-Herrero, D. Efetov, P. Kim, Electronic transport in locally gated graphene nanoconstrictions. *Appl. Phys. Lett.* **91**, 192107 (2007).
57. S. Deng, E. Gao, Y. Wang, S. Sen, S. T. Sreenivasan, S. Behura, P. Král, Z. Xu, V. Berry, Confined, oriented, and electrically anisotropic graphene wrinkles on bacteria. *ACS Nano* **10**, 8403–8412 (2016).
58. S. Plimpton, Fast parallel algorithms for short-range molecular dynamics. *J. Comput. Phys.* **117**, 1–19 (1995).
59. K. Vanommeslaeghe, E. Hatcher, C. Acharya, S. Kundu, S. Zhong, J. Shim, E. Darian; O. Guvench, P. Lopes, I. Vorobyov, A. D. Mackerell, CHARMM general force field: A force field for drug-like molecules compatible with the CHARMM all-atom additive biological force fields. *J. Comput. Chem.* **31**, 671–690 (2010).
60. W. Yu, X. He, K. Vanommeslaeghe, A. D. MacKerell Jr., Extension of the CHARMM general force field to sulfonyl-containing compounds and its utility in biomolecular simulations. *J. Comput. Chem.* **33**, 2451–2468 (2012).

Acknowledgments: We thank J. V. Pagaduan and Q. Jin for help with the cell culture and J. Liu for the discussions of theoretical models. **Funding:** This work was supported by the Air Force Office of Scientific Research MURI (Multidisciplinary University Research Initiative) program (FA9550-16-1-0031 and FA9550-15-1-0514), the National Science Foundation (CMMI-1635443), and the Office of Naval Research (N00014-16-1-2333). This work also used the Extreme Science and Engineering Discovery Environment, which is supported by the National Science Foundation (ACI-1053575). This research was performed in part at NIST (National Institute of Standards and Technology) Center for Nanoscale Science and Technology. **Author contributions:** W.X. and D.H.G. conceived and designed the experiments. W.X. carried out most of the experiments and analyzed the data. Z.Q., C.-T.C., and M.J.B. conducted the modeling and theoretical analysis of the folding. H.R.K and A.S. helped with the fabrication process. Q.M. helped with the electrical measurements. All the authors discussed the results and wrote the manuscript. **Competing interests:** The authors declare that they have no competing interests. **Data and materials availability:** All data needed to evaluate the conclusions in the paper are present in the paper and/or the Supplementary Materials. Additional data related to this paper may be requested from the authors.

Submitted 6 April 2017
Accepted 12 September 2017
Published 6 October 2017
10.1126/sciadv.1701084

Citation: W. Xu, Z. Qin, C.-T. Chen, H. R. Kwag, Q. Ma, A. Sarkar, M. J. Buehler, D. H. Gracias, Ultrathin thermoresponsive self-folding 3D graphene. *Sci. Adv.* **3**, e1701084 (2017).

Science Advances

AAAS

advances.sciencemag.org/cgi/content/full/3/10/e1701084/DC1

Supplementary Materials for

Ultrathin thermoresponsive self-folding 3D graphene

Weinan Xu, Zhao Qin, Chun-Teh Chen, Hye Rin Kwag, Qinli Ma,
Anjishnu Sarkar, Markus J. Buehler, David H. Gracias

Published 6 October 2017, *Sci. Adv.* **3**, e1701084 (2017)
DOI: 10.1126/sciadv.1701084

This PDF file includes:

- fig. S13. Single cell encapsulation and Raman study.
- fig. S14. Initial configuration of the PNIPAM-water system in the MD model.
- fig. S15. Top view of the aggregation behavior of an array of (36 chains in total) PNIPAM brushes at different temperatures in MD simulations.
- fig. S16. Comparison between the coarse-grained MD model and the experiment results for a functionalized graphene flower with different size.
- fig. S17. The effect of mechanical properties of the two layers on self-folding.
- fig. S18. Electrical measurements on pristine graphene and functionalized graphene dumbbell.
- fig. S19. Dimension of the folding crease measured by AFM.
- fig. S20. Output and transfer curves of the pristine and functionalized graphene FET.
- table S1. XPS data analysis of graphene, G-PD, and G-PD-PNIPAM at the C1s, N1s, and O1s peaks.
- table S2. Tensile test results of PNIPAM from the MD simulations.

1. Additional experimental details

1.1. Preparation of the patterned Al/Si substrate and graphene transfer

The substrates used in all our experiments were composed of a silicon (Si) wafer with a thermally grown 300 nm thick oxide (SiO_2) film. In order to enable the selective attachment of graphene to the substrate *via* van der Waals forces, a patterned Al layer was deposited on top of the SiO_2 using lift-off metallization. Briefly, the SiO_2/Si wafer was first patterned by photolithography, leaving a patterned layer of photoresist (SC 1827 MicroChem) on the surface. Then a thin layer of Al (40 nm) was thermally evaporated on the surface. The photoresist was dissolved in acetone, leaving behind a patterned layer of Al on the SiO_2/Si wafer.

CVD monolayer graphene was purchased from Graphene Supermarket (Reading, MA, USA), and was transferred onto the patterned substrates using the PMMA transfer method. Briefly, a layer of PMMA (Sigma Aldrich, M_w: 996,000) was spin coated on the graphene, and after thermal annealing, graphene on the other side of the copper foil was removed using an oxygen plasma. Then, the graphene/PMMA film on the copper foil was placed into an aqueous iron chloride ($FeCl_3$) solution (1 mol/L) to etch away the copper. The PMMA/graphene films were washed with deionized water (twice) followed by hydrochloric acid (10%) and then deionized water (thrice) to remove any residual ions. Subsequently, the graphene/PMMA films were transferred onto the patterned substrate, and the PMMA layer was dissolved by immersion in acetone for 6 h.

1.2. Cell culture and encapsulation

The breast cancer cell line MDA-MB-231 (ATCC, Manassas, VA, USA) was used in this work. Cells were grown in DMEM media supplemented with 10% fetal bovine serum (FBS) and 1% penicillin-streptomycin in a humidified incubator at 37 ^oC and 5% CO_2. The live/dead assay was performed by incubating the cells with calcein AM and ethidium homodimer-1 (Thermo Fisher Scientific, Rochester, NY, USA) in PBS solution at 37 ^oC for 30 min. The cells were then examined under a confocal microscope (Zeiss LSM 510).

For the encapsulation of cells with graphene, the cells were trypsinized and suspended in fresh culture media. Then a certain amount of the cell suspension was added to a Petri dish which contains the substrate with functionalized graphene microstructures on it. The elevated temperature during cell culture (37 ^oC) induces the folding of the functionalized graphene structures, which can encapsulate the cells inside.

2. Raman spectra of the functionalized graphene

After surface functionalization with PD and PNIPAM, peaks at 1350 and 1591 cm^{-1} broaden, which can be attributed to the presence of PD. The intensity of these peaks increases with increasing PD functionalization time suggesting formation of a thicker film. The reference spectra of PD with two different thickness on a bare silicon substrate is shown in fig. S1. PNIPAM does not show a measurable Raman signal in comparison to the signal of PD and graphene at the wavenumber range studied.

PD itself exhibits two broad weak peaks at 1350 and 1580 cm^{-1} in Raman (fig. S1), which correspond to the stretching and deformation of the aromatic rings. After depositing PD on the surface of graphene, it can be seen that there is an increase in the D band intensity. Based on the overlapping peaks with PD, we believe that this increase is due to PD and not due to defects in graphene. The shape and intensity of the G band changes after PD deposition: pristine graphene has a sharp peak, while for G-PD the bottom part of the peak becomes broader; there is also a small increase in G band intensity. Such effects become more significant with an increase of PD layer thickness, as can be seen from Raman of G-PD2 and G-PD4 (dopamine polymerization for 2 hours and 4 hours, respectively).

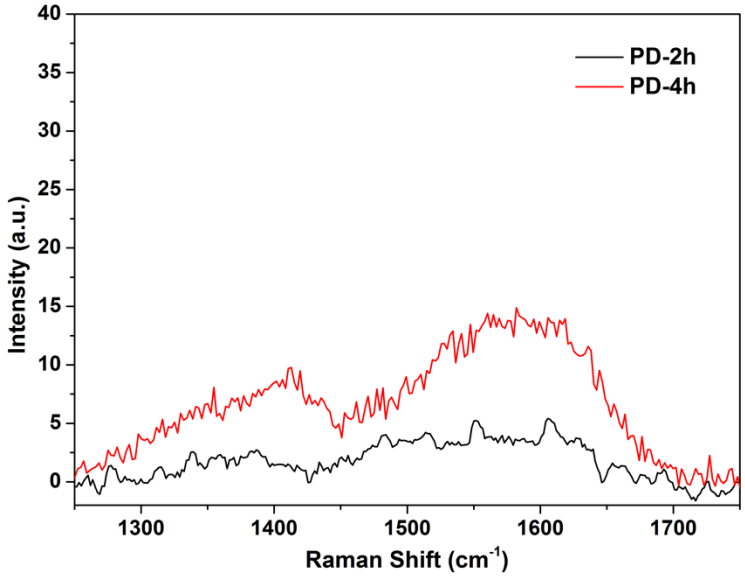

fig. S1. Raman spectra of PD with different thickness (self-polymerization for 2 and 4 hours) on the Si substrate.

3. AFM characterization of the functionalized graphene

The thickness and surface morphology of the functionalized graphene were studied by atomic force microscopy (AFM) (fig. S2). The line scans indicate that the pristine graphene on the Si substrate has a thickness of 0.8 nm, and after PD deposition, the thickness increases to 6.0 and 6.9 nm for G-PD2 and G-PD4, respectively. The surface of G-PD is smooth and uniform, which indicates the strong and intimate interaction between PD and graphene. After further grafting of PNIPAM, the thickness of the G-PD-PNIPAM further increases to 8.5, 8.9 and 9.6 nm for grafting reaction of 12h, 18h, and 24h.

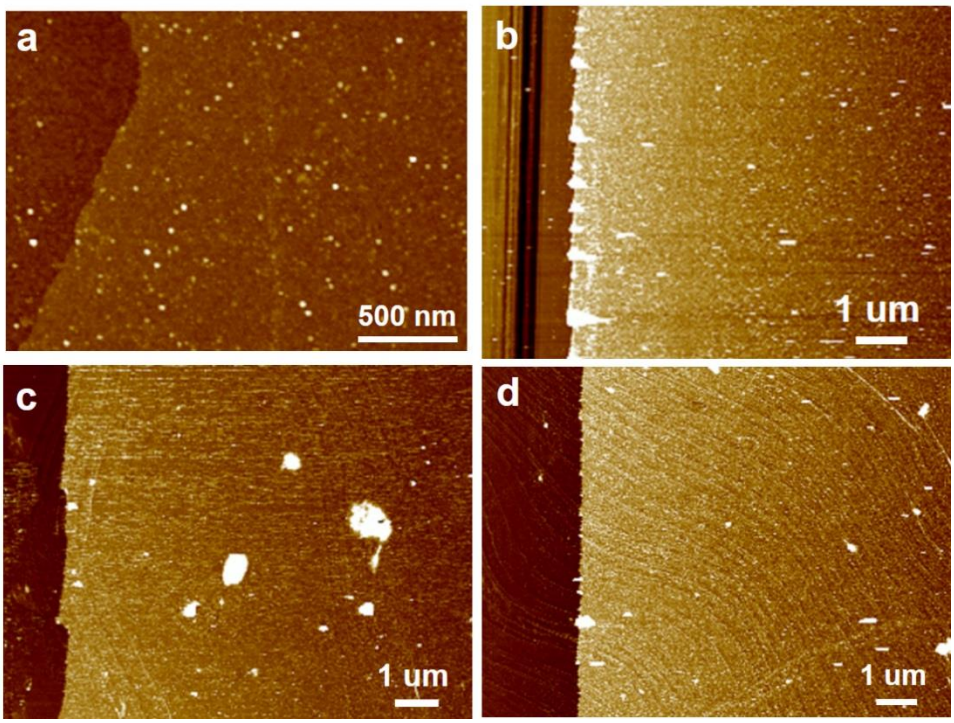

fig. S2. Surface morphology of graphene and functionalized graphene. AFM images of pristine graphene (**a**). G-PD4 (**b**), G-PD2-PNIPAM12 (**c**), and G-PD2-PNIPAM24 (**d**). Z range is 20 nm.

4. XPS characterization of functionalized graphene

The chemical composition of the functionalized graphene was characterized by X-ray Photoelectron Spectroscopy (XPS). Fig. S3 shows the XPS survey spectra for graphene, G-PD, and G-PD-PNIPAM, which were collected over the binding energy (B.E.) range from 0 to 1100 eV with a step size of 1 eV. It can be seen that the C1s and O1s peak exist for all three samples, G-PD and G-PD-PNIPAM have an additional N1s peak, while pure graphene does not, and the N1s peak intensity is stronger for G-PD-PNIPAM, which proves the successful deposition of PD and subsequent grafting of PNIPAM on the surface of graphene.

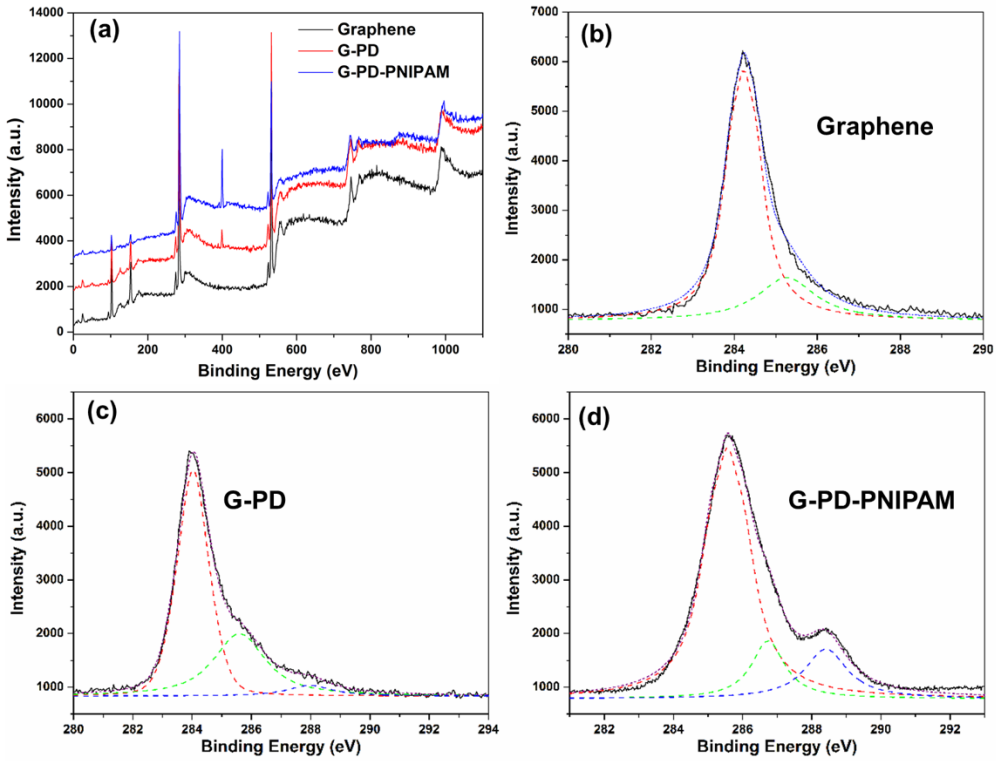

fig. S3. Chemical composition of functionalized graphene studied by XPS. (**a**) XPS spectra of graphene and functionalized graphene on SiO_2/Si substrate. High resolution C1s XPS spectrum and peak fitting of (**b**) graphene, (**c**), G-PD, and (**d**) G-PD-PNIPAM.

For the graphene sample, the C1s peak can be decomposed into two apparent spectral components at 284.2 and 285.3 eV (fig. S3b), the main peak at 284.2 eV corresponds to the graphite-like sp^2 carbon, and the small peak at 285.3 eV is the sp^3 carbon from defects and edge of the graphene, and the energy difference between sp^2 and sp^3 carbon atoms is 0.9 eV. The C1s peak for G-PD can be deconvoluted into three component (fig. S3c): sp^2 C-H on the aromatic rings at 284.0 eV, which is the major one; C-O/ C-N species at 285.6 eV, and C=O/C=N species at 287.9 eV (table S1). After PNIPAM grafting, the C1s peak has an obvious change in shape and position, it can be decomposed into three peaks, the major one at

285.6 eV for CH_x, another one at 286.7 eV for C-C=O groups, and a third one at 288.4 eV for N-C=O groups.

table S1. XPS data analysis of graphene, G-PD, and G-PD-PNIPAM at the C1s, N1s, and O1s peaks.

Sample	C1s			N1s			O1s		
	group	BE (eV)	percent	group	BE (eV)	percent	group	BE (eV)	percent
Graphene	sp^2 C	284.2	78.7%						
	sp^3 C	285.3	21.3%						
G-PD	CH_x (sp^2)	284.0	62.9%	R-NH_2	399.5	88.2%	O=C	532.7	92.8%
	C-O / C-N	285.6	32.2%	R_2-NH	400.5	11.8%	O-C	531.1	7.2%
	C=O / C=N	287.9	4.9%						
G-PD-PNIPAM	CH_x (sp^3)	285.6	72.3%	R_2-NH	400.5	100%	O=C	532.4	100%
	C-C=O	286.7	13.3%						
	N-C=O	288.4	14.4%						

The O1s peak (fig. S4) exists for graphene sample, which comes from the SiO_2 substrate underneath, and the peak can be fitted with a single peak at 532.9 eV (SiO_2). For G-PD, the O1s region is fit with two peaks assigned to O=C and O−C species, which are located at 532.7 and 531.1 eV, respectively (table S1), with the former being the majority. For G-PD-PNIPAM, with the grafting of PNIPAM, there is only one peak at 532.4 eV, which corresponds to O=C groups.

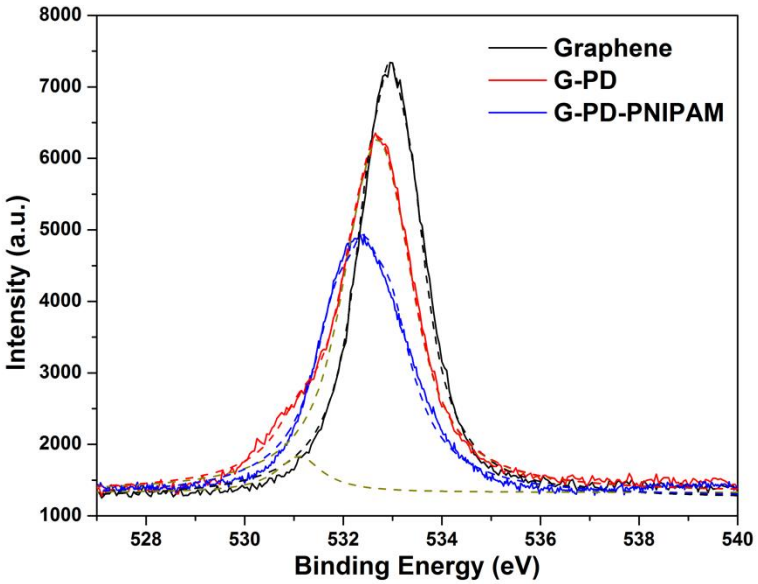

fig. S4. High-resolution O1s XPS spectra and peak fitting (dotted lines) of graphene, G-PD, and G-PD-PNIPAM.

Figure 2D shows the N1s high resolution spectrum. There is no peak exist for graphene because of the lack of the nitrogen element in graphene. For G-PD the peak can be deconvoluted and fitted with two peaks centering at 399.5 eV and 400.5 eV, which can be assigned to the primary amine and secondly amine , respectively, with the primary amine groups constituting the major contribution for polydopamine. The N1s peak for G-PD-PNIPAM has a much higher intensity, and can be fitted with one peak centering at 400.5 eV, because the grafted PNIPAM chains have higher nitrogen content and only secondary amine groups. The overall element ratio of graphene after polydopamine deposition and subsequent PNIPAM grafting changes significantly. For instance, the N:C:O ratio is 1: 18.1: 9.1 for G-PD, and 1: 7.0: 2.1 for G-PD-PNIPAM. All of the surface analysis data confirm the surface modification of graphene with PD and PNIPAM.

5. Optical and SEM imaging of the self-folding graphene structures

In the experiment, we placed a rigid SU-8 epoxy hinge in the center of the top two faces, in order to separate them and induce the folding of a closed box, in which the top face will be the lid. The length of the SU-8 hinge is the same as one side of the box (200 µm), the width of the hinge is 25 µm, and the thickness is around 300 nm. Since the width of the SU-8 hinge is small compared with the size of the face, it simply acts as a rigid hinge, and we found that variation of the hinge width does not significantly affect the extent of folding when it is thin. For instance, a box with the same materials and dimension, but with a SU-8 hinge of 12.5 µm wide show very similar folding behaviors as that of the original samples (25 µm wide hinge; Fig. 3, G to I in the main text), as shown in fig. S5 a to c. On the other hand, using coarse-grained molecular dynamics (MD) models, we found that when the hinge width becomes quite large (above 40 µm), it will affect the folding of the top two faces, as shown in fig S5 (d to f).

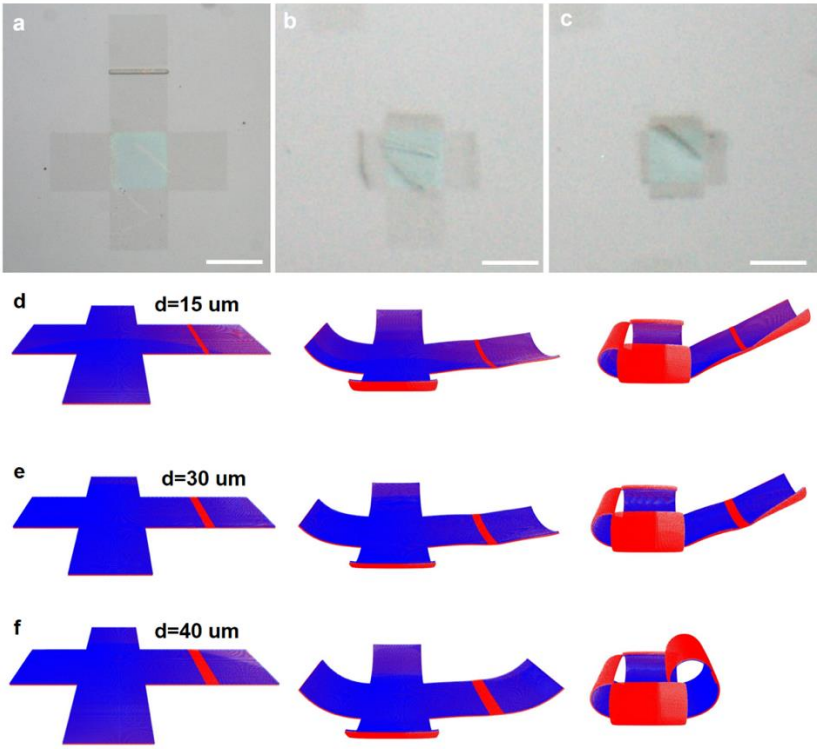

fig. S5. Effect of the rigid hinge on the self-folding of functionalized graphene box. (a to **c)** Self-folding process of a functionalized graphene box with a 12.5 µm wide hinge, panels a, b, c corresponds to the sample before, during and after folding, respectively. The scale bars are 200 µm. (**d** to **f**) The self-folding process of a graphene box with different hinge widths (15, 30 and 40 µm), obtained from coarse-grained MD model. When the hinge width is thin, the folding is not significantly affected but when the width increases the folding can be affected.

SEM images of the representative folded structure in the dry state are shown in fig. S6, it can be seen that the functionalized graphene microstructures are stable and uniform, and tend to collapse onto the substrate upon drying.

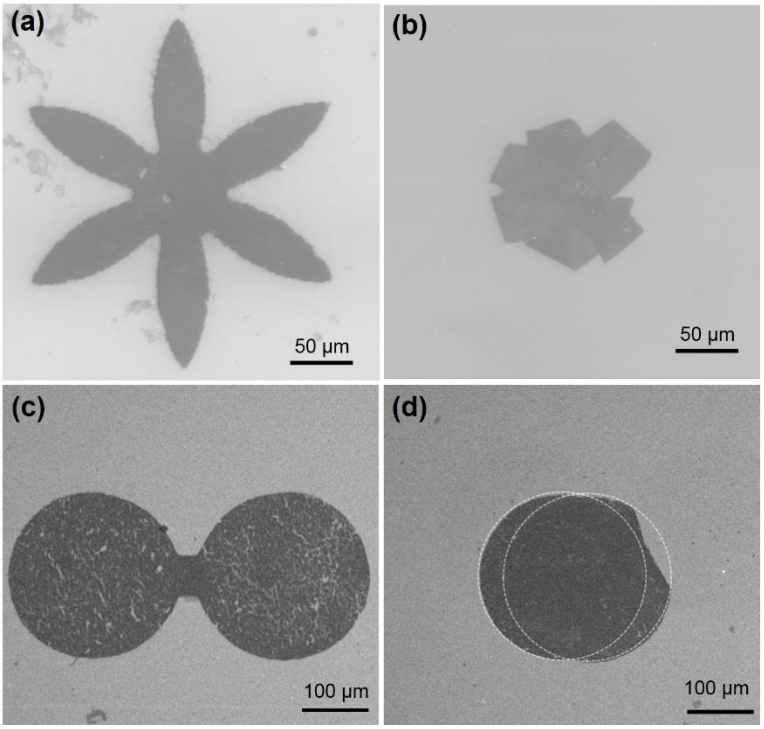

fig. S6. Characterization of the self-folding graphene microstructures using SEM. SEM images of the G-PD-PNIPAM flower (**a** and **b**) and dumbbell (**c** and **d**), before and after folding, the white circles in panel d represents the outlines of the two graphene disks in the dumbbell.

To show that the temperature induced self-folding process has high efficiency and high yield, optical images of a large area of the graphene flowers during folding are shown in fig. S7, which demonstrates the parallel and high throughput nature of our process. Moreover, to prove that the folding of the functionalized graphene is induced by PNIPAM chains contraction at elevated temperature, we also performed a controlled experiment with a patterned pristine graphene dumbbell and a G-PD dumbbell at the same condition, and both of the two samples do not show self-folding behavior at increased temperature due to the absence of PNIPAM brushes (fig. S8).

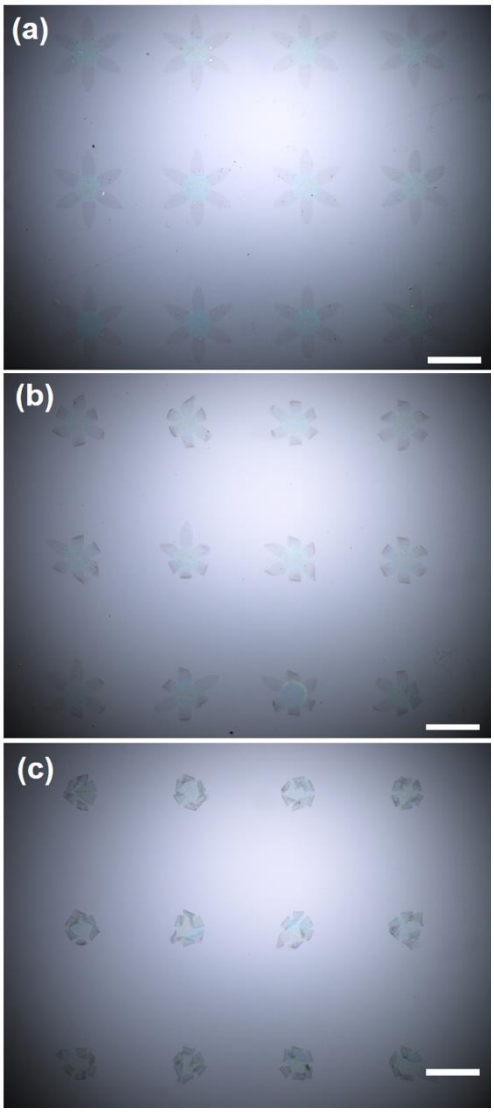

fig. S7. Highly parallel self-folding of ultrathin 3D graphene microstructures. Optical microscope images of a large area of graphene flowers before (**a**), during (**b**) and after (**c**) self-folding induced by temperature increase. Scale bars are 200 μm.

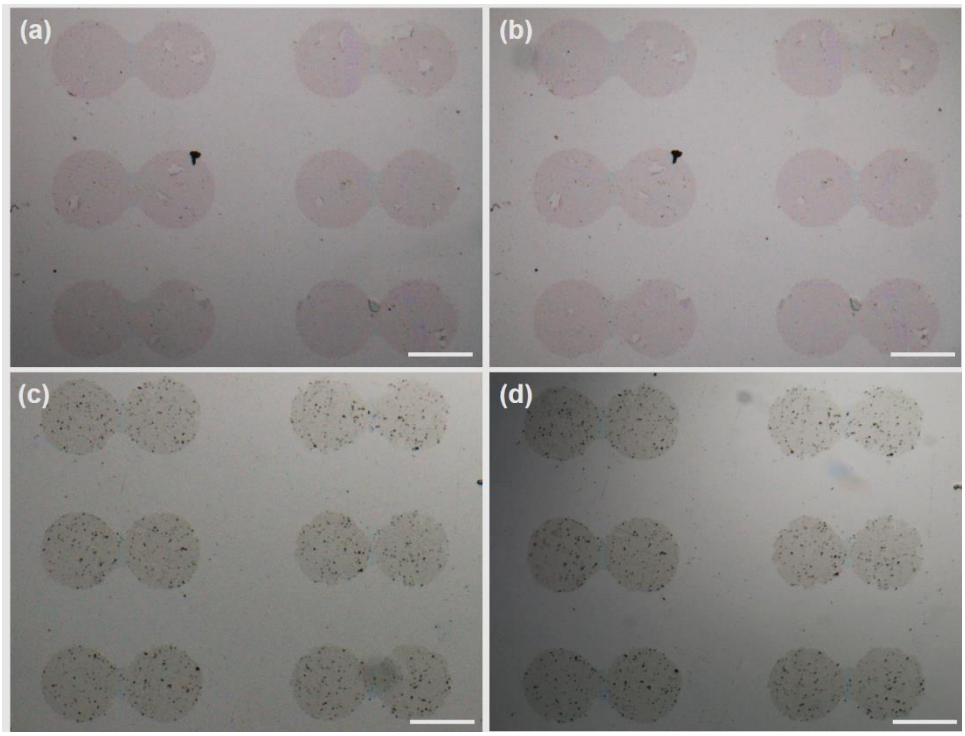

fig. S8. Control experiments of self-folding on pristine graphene and G-PD. Optical microscope images of pristine graphene dumbbells (**a** and **b**) and G-PD dumbbells (**c** and **d**) at room temperature (left column) and after heating to 45 °C (right column), both samples do not show self-folding behavior. Scale bars are 200 μm.

The thickness of the functionalized graphene can be further decreased by reducing the polymerization time of PD, as well as the grafting time of PNIPAM brushes. For instance, with a PD polymerization time of 1h, and PNIPAM grafting time of 3h, we are able to reduce the total thickness to 5 nm (fig. S9a). Moreover, the thinner functionalized graphene is still temperature responsive and self-folding can be achieved (fig. S9).

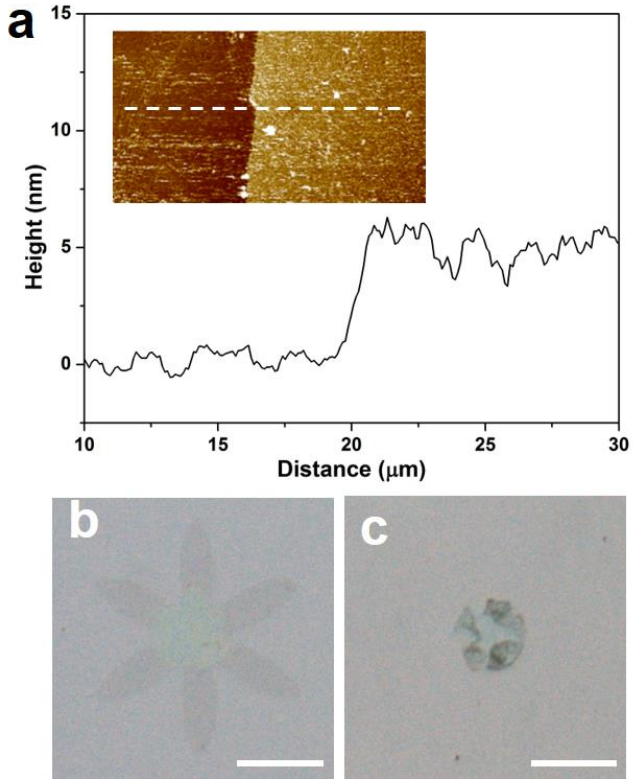

fig. S9. Self-folding of functionalized graphene with 5 nm thickness. (**a**) Thickness measurement of the G-PD-PNIPAM sample with reduced thickness, inset is the AFM height image. (**b** to **c**) Self-folding of the thin functionalized graphene flower with increasing temperature. Scale bars are 100 μm.

Temperature can be used to control the folding extent for simple and regular shaped functionalized graphene microstructures at certain temperature range. As shown in fig. S10, we studied the folding process of a half-functionalized graphene dumbbell, panel a is the original flat state, and panels b-f correspond to temperature of 35ºC, 38ºC, 41ºC, 43 ºC and 46 ºC, respectively. Within this temperature range, the higher the temperature, the higher the extent of folding can be achieved. But it needs to be noted that even higher temperature (above 45 ºC) does not have significant difference to the folding compared with that of 45 ºC, because it is already well above the LCST of PNIPAM.

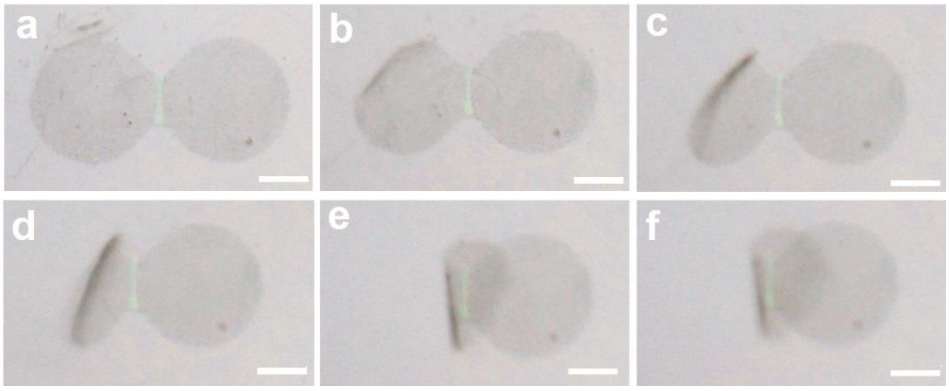

fig. S10. The folding process of half-functionalized graphene dumbbell with increasing temperature. From a–f the solution temperature is 25, 35, 38, 41, 43 and 46 °C, respectively. All scale bars are 100 μm.

6. Raman spectra of folded graphene

In order to show that the graphene retains its molecular structure and high quality in the temperature induced folding process, Raman spectroscopy was used to characterize the folded microstructures. As shown in fig. S11, which is a folded graphene flower in the dry state, and Raman spectra were collected at two representative spots, one is in the unfolded monolayer region, and the other is in the folded bilayer region. It can be seen that Raman spectra of both spots have a sharp G and 2D band, with a weak D band. The intensity of both G band and 2D bands have an obvious increase for the folded region, and the I_{2D}/I_G ratio increases from 1.78 at the flat region to 2.27 at the folded bilayer region. Moreover, the position of the G and 2D band have almost no change before and after folding, which is quite different from previous reports on bilayer graphene when the two layers are in intimate contact (the 2D band of bilayer graphene is blue-shifted relative to monolayer graphene, with the blue-shift magnitude depending nonmonotonically on the rotation angle), the main reason is the PD and PNIPAM brushes in between the two graphene layers eliminate their strong interaction.

Moreover, the D band does not change for the folded region, which is quite different from previously reported folded graphene, and means the folding process does not induce additional defects, the interaction between the two graphene layers is screened by the thin polymer layer in between. When graphene folded directly on itself, there will be a second peak in the D band region, which has been called the I band. This is a nondispersive peak that arises from a weak but well-ordered perturbation caused by the folded layer upon the parent layer. In our case, due to the existence of a thin polymer layer in between the folded graphene, such a perturbation is largely eliminated, so the I band is not present here.

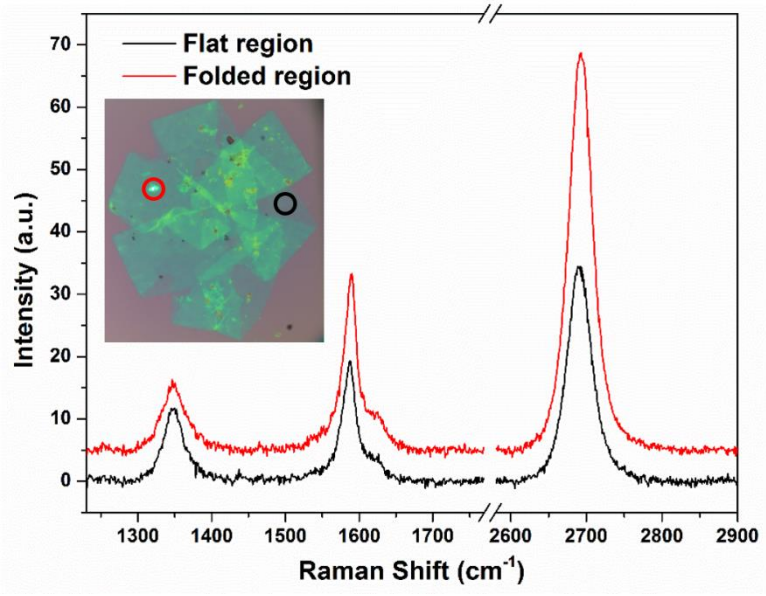

fig. S11. Raman spectra of a graphene flower in the flat and folded regions. The inset is the optical microscopy image taken with the Raman microscope. The black and red circles indicate flat and folded regions where the spectra were taken.

7. Cell encapsulation and Raman analysis

Self-folding graphene microstructures have promising biomedical applications due to their ultrathin nature, pliability and good biocompatibility. As an example, self-folding graphene flowers were used as soft grippers to encapsulate live cells. Pristine graphene itself is very hydrophobic, and the cell adhesion on it is not as good as bare glass substrate. As shown in fig. S12a, the cell density is lower on pristine graphene, but all the cells are alive on graphene, which indicates its good biocompatibility. On the other hand, after surface functionalization with PD and PNIPAM, which increases the hydrophilicity, the G-PD-PNIPAM shows increased cell density indicating excellent cell adhesion in addition to biocompatibility (fig. S12b).

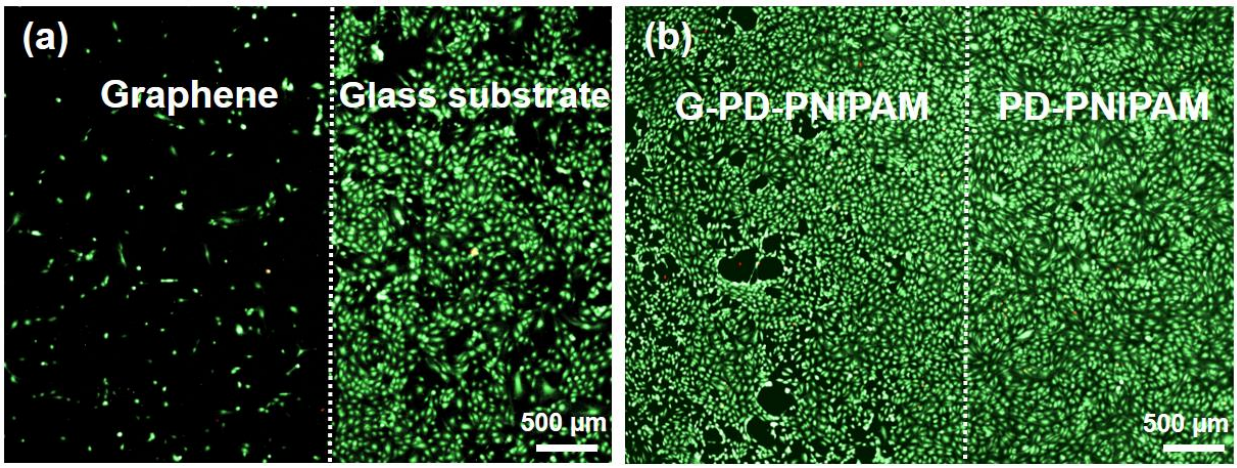

fig. S12. Cell viability with the live/dead assay. (**a**) Representative fluorescent image of the cells on graphene, live cells were stained green (calcein AM) while dead cells were stained red (ethidium homodimer). (**b**) Representative fluorescent image of the cells on functionalized graphene (G-PD-PNIPAM).

After encapsulation with the ultrathin graphene, we performed a Raman study on the encapsulated live cell, and the results showed that the Raman signals from the relevant biological molecules in the cell are significantly enhanced, which is useful for biosensing and biodetection. More specifically, as shown in fig. S13, for flat G-PD-PNIPAM, there are two main peaks, G and at 1590 cm^{-1}, and 2D band at 2638 cm^{-1}; as well as a weak D band at 1350 cm^{-1}. As a control, the folded functionalized graphene without cell inside show similar peaks, with an increase in G and 2D band intensity.

After encapsulation of the cell inside the functionalized graphene, there are pronounced changes and new peaks in the Raman spectrum. For instance, the $N^{+}(CH_3)_3$ symmetric stretch vibrations of the choline moiety at 711 cm^{-1} are observed. This is a characteristic peak for phospholipids, one of the major constituents of cellular membranes. The ring breathing modes in the DNA and RNA bases at 786 cm^{-1},

and the symmetric O-P-O stretching vibrations in RNA at 808 $cm^{-1}$are observed; both of which are located in the nuclei of the cells. The symmetric breathing mode of phenylalanine at 1003 cm^{-1}, which is a typical Raman feature for proteins is also present. The peak at 1450 cm^{-1} peak corresponds to CH_2 deformation from phospholipids and proteins. Moreover, there is a shoulder peak at 1610 cm^{-1}, which corresponds to phenylalanine, a major component of proteins. There is also a large increase in the G band and 2D band intensity, and the former is due to phenylalanine, the latter one comes from the different biomolecules (such as proteins) in the cell. The D band intensity also significantly increased after cell encapsulation, which indicates an intimate contact and interaction between graphene and the cell which induces some extent of structural changes and defects to graphene.

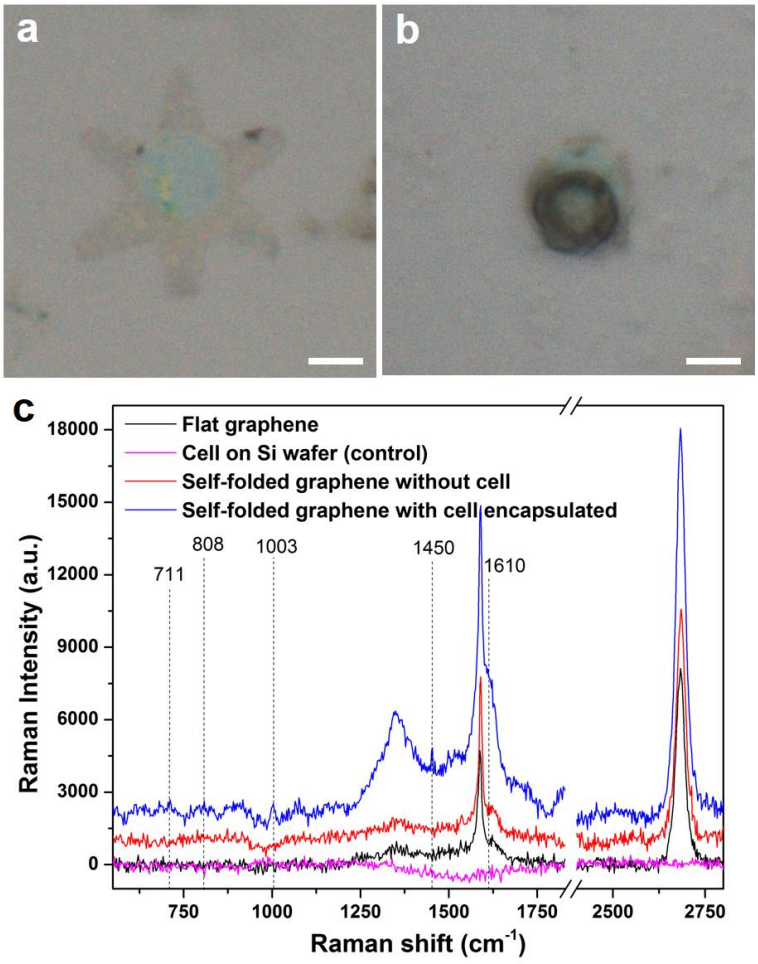

fig. S13. Single cell encapsulation and Raman study. A functionalized graphene flowers in flat state (**a**), and after encapsulation of a single breast cancer cell (**b**). (**c**) Raman spectra of functionalized graphene and after its encapsulation of a breast cancer cell. Scale bars are 10 μm.

8. Full atomistic modeling of the folding behaviors

Since both the PD and PNIPAM layers are very thin (i.e., 3~5 nm in the dry state), it is difficult to measure their mechanical properties experimentally with high accuracy, especially in an aqueous condition where the folding is conducted. We have carried out a full atomistic computational study on PNIPAM and PD using MD simulations (details in the Method part) to supplement our experimental work and provide the required coefficients for our coarse-grained MD model.

8.1. Estimation of PNIPAM's volume

PNIPAM always absorbs a certain amount of water, and thus the volume of PNIPAM includes the volume of the surrounding water. After the MD equilibration, the coordinates of the PNIPAM chains as well as the surrounding water molecules (within a cutoff of 5 Å) were used to estimate the volume of the PNIPAM aggregate in the system. The triangular surface plot in MATLAB was applied to generate a surface of the PNIPAM aggregate based on these coordinates. As the surface of the PNIPAM aggregate is defined, its volume can be calculated.

8.2. Estimation of PNIPAM's Young's modulus

After the MD equilibration, the extra water molecules (larger than a cutoff of 5 Å) were removed from the PNIPAM-water systems (i.e., at 275 K and 325 K), and the systems were then equilibrated with the NPT ensemble at a constant temperature of 275 K and 325 K for another 10 ns, respectively. The pressure was set to 1.013 bar in all three directions. The constrain at the bottom part of each PNIPAM chain was released to prevent obtaining unreasonable results from tensile tests, which were performed to estimate the modules of PNIPAM. A tensile stress of 10 MPa was applied to the PNIPAM-water systems (with extra water molecules removed) in the *y*- or *z*-directions and the corresponding tensile strain was measured with the NPT ensemble at a constant temperature of 275 K and 325 K for 1.0 ns, respectively. Except for the stretching direction, where the tensile stress was applied, the pressures in the other two directions were set to 1.013 bar. The Young's modulus of PNIPAM was estimated as the ratio of the applied tensile stress and corresponding tensile strain.

8.3. Coarse-grained modeling and equilibration

Each layer of the composite membrane material is modeled by an elastic network with carefully chosen elastic constants to match the materials' elastic properties and mass concentrated at the junction beads to match the material densities, such a strategy has been proven to be efficient to model other biological materials. It is noted that both the bond length and stiffness constant change only apply to the PNIPAM layer while these parameters for the graphene and PD layer are kept constant through the simulation.

We used the FCC lattice to model the location of the mass beads (which locate at corners and face centers) and used an elastic spring to model the interaction between the nearest neighboring beads. The total energy function is given by

$$E = E_T = \sum \varphi_T(r) \tag{1}$$

where E_T is the deformation energy for stretching/compression of all the springs. Each energy term was defined by

$$\varphi_T(r) = k(r - r_0)^2 \tag{2}$$

where $2k$ is the spring stiffness, $r_0 = a/\sqrt{2}$ is the equilibrium distance between two neighboring beads and a is the lattice constant of the FCC lattice. By assuming the polymers have Poisson ratio of ν=0.25, the Young's modulus E of such material composed of FCC lattice and elastic springs is given by

$$E = \frac{16k}{3a} \tag{3}$$

where E is the Young's modulus. The bending stiffness the PD layer of l=5 nm in thickness is given by $D = EI = E\frac{l^3}{12} = 52$ nN·nm, given the fact that the Young's modulus of PD material is E=5 GPa, which is obtained from the full atomistic MD simulations and experiments. It is noted that such stiffness is two orders of magnitude higher than the bending stiffness of a single layer of graphene as 0.15 nN·nm for a unit width of graphene and thus we do not explicitly model graphene in this coarse-grained model.

Considering the fact that the membrane is extremely thin as the two dimensions in the in-plane directions (>100 μm) are more than four orders of magnitudes larger than the membrane thickness (5 nm) and for the sake of simplicity of the numerical model and a smaller number of total coarse-grained beads. We scale up the thickness in the coarse-grained model to a length same as the lattice constant of $l=a$ but scale down the k value to keep the bending stiffness to be the same for each layer. Therefore, we have

$$k\,(t) = \frac{9D(t)}{4a^2} \tag{4}$$

where D is the bending stiffness of each of the two layers, evolving as a function of time simply as $D(t) = D_{end} + (D_0 - D_{end})\exp(-\frac{t}{t_0})$, where D_0 is the bending stiffness at low temperature at beginning and D_{end} is the bending stiffness at high temperature, t_0 is a time constant with its numerical value of 2 s applied to all of our coarse-grained simulations. In the simulation of the coarse-grained model, we also

implicitly simulate the effect of the temperature on PNIPAM brushes layer by tuning the equilibrium length constant of the lattice structure as

$$a\,(t) = a_{end} + (a_0 - a_{end})\exp(-\frac{t}{t_0}) \quad (5)$$

where $a_0 = 4$ μm is the initial lattice length at low temperature, $a_{end} = 0.71a_0$ is the equilibrium length constant at high temperature, which reflects the 49% in-plane volume change for one length dimension, and t_0 is the time constant used in simulations to reflect how quick the PNIPAM responds to the temperature change.

8.4. Modeling of the folding behaviors

Since there is covalent bonding between PD and PNIPAM brushes, one end of the PNIPAM chains is fixed to the PD layer. To mimic this mechanical boundary condition, the bottom part of each PNIPAM chain is fixed in the x-direction (fig. S14). As a result, the bottom part of each PNIPAM chain cannot move in the x-direction but is free to move in the other two directions. The 12-6 Lennard-Jones interactions and Coulombic interactions were computed with a cutoff of 8 Å and 10 Å, respectively. The long-range interactions were calculated with a particle-particle particle-mesh solver (pppm). The integration time step was set to 1.0 fs.

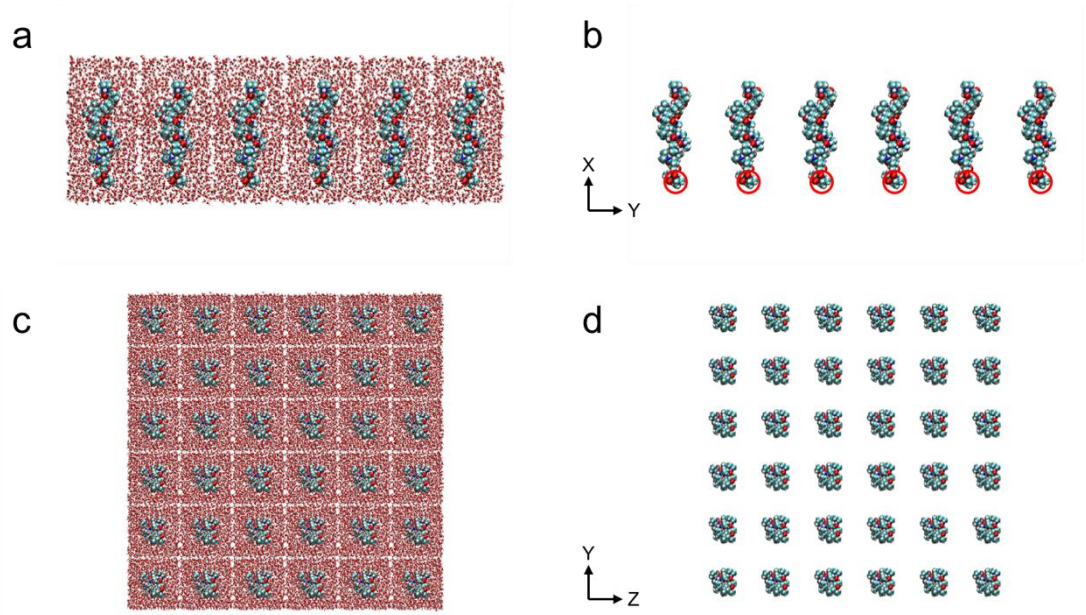

fig. S14. Initial configuration of the PNIPAM-water system in the MD model. The PNIPAM model consists of 36 PNIPAM chains with a chain length of 20-mer. The longitude direction of each PNIPAM chain is faced to the *x*-direction of the simulation box, and the PNIPAM chains are separated with a distance of 30 Å in both the *y*- and *z*-directions. The mass of the PNIPAM chains is around 10% of the mass of the water molecules. The initial configuration in the *x*-*y* direction is shown in (**a**) as well as (**b**), in which water is not shown for clarity. The initial configuration in the *y*-*z* direction is shown in (**c**) as well as (**d**), in which water is not shown for clarity. The red circles in (b) indicate the bottom part of each PNIPAM chain, which is fixed during the equilibration.

Figure S15a show the equilibrium structures of an array of 36 PNIPAM brushes at 275 K. When the temperature is lower than LCST, the PNIPAM chains are in the swollen hydrated state, which absorbs a large amount of water around the polymer chains. The volume of the PNIPAM aggregate was calculated as the sum of the volume of the PNIPAM chains and the volume of the surrounding water. The surface of the PNIPAM aggregate is shown in fig. S15b and the volume is around 308 nm^3. On the other hand, when the temperature is higher than LCST, the PNIPAM chains are in the shrunken dehydrated state, which are mostly hydrophobic. Fig. S15c show the equilibrium structures of the PNIPAM brushes at 325 K and the surface of the PNIPAM aggregate is shown in fig. S15d. Due to the fact that a large amount of water is lost at 325 K, the volume of the PNIPAM aggregate is decreased to around 157 nm^3, which is only 51% of the volume at 275 K.

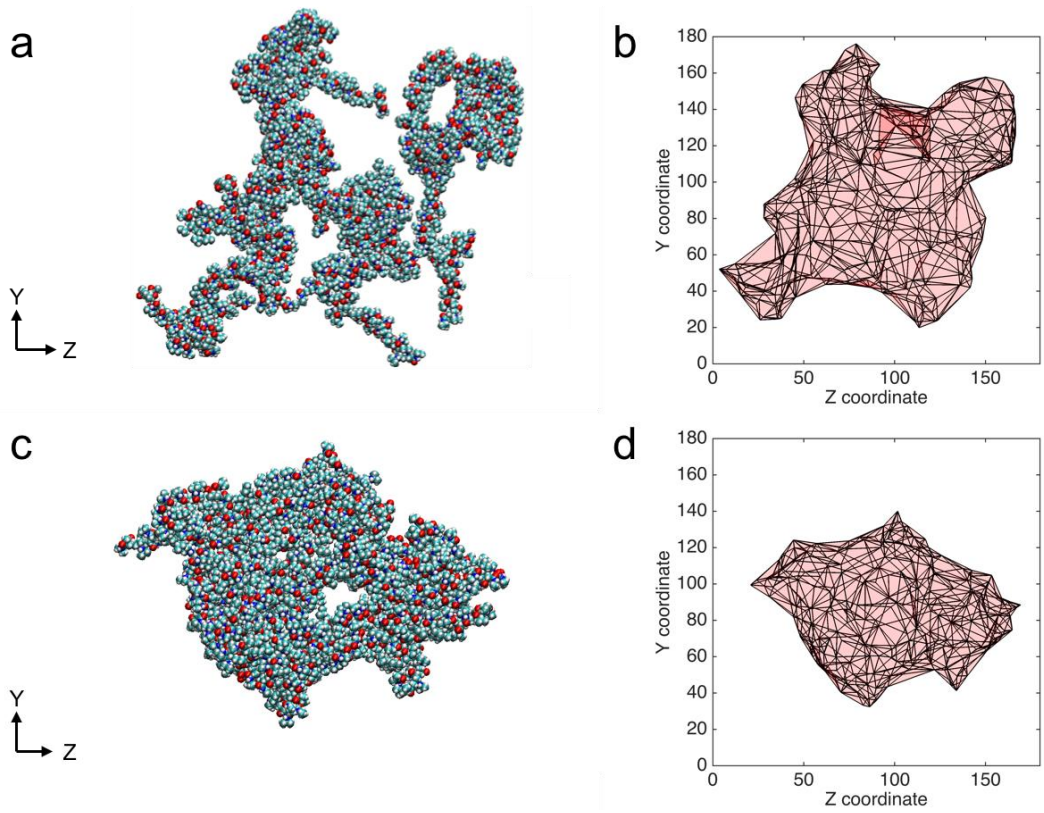

fig. S15. Top view of the aggregation behavior of an array of (36 chains in total) PNIPAM brushes at different temperatures in MD simulations. (**a**) The equilibrium structure of PNIPAN brushes at 275 K and (**b**) the surface of the aggregate. (**c**) The equilibrium structure of PNIPAN brushes at 325 K and (**d**) the surface of the aggregate. Water is not shown in (a) and (c) for clarity.

In this study, tensile tests were performed to estimate the Young's modulus of PNIPAM. The tensile test results are shown in table S2. Since the self-folding mechanism of the graphene microstructures is caused by the in-plane (*y*- and *z*- directions) stresses of PNIPAM, only the in-plane Young's moduli are calculated. At a temperature of 275 K, the Young's moduli of PNIPAM are calculated as 87 MPa and 101 MPa in the *y*- and *z*- directions, respectively, resulting in an average of ~94 MPa. On the other hand, at a temperature of 325 K, the Young's moduli of PNIPAM are calculated as 221 MPa and 265 MPa in the *y*- and *z*- directions, respectively, resulting in an average of ~243 MPa. As the temperature difference is only 50 K, which has a negligible effect on the intrinsic Young's modulus, the difference between the Young's moduli at different temperatures is mainly caused by the structural transformation of the PNIPAM chains.

table S2. Tensile test results of PNIPAM from the MD simulations. The Young's moduli of PNIPAM is calculated as ~94 MPa and ~234 MPa at 275 K and 325 K, respectively.

System	L_X (Å)	L_Y (Å)	L_Z (Å)	S_{XX} (MPa)	S_{YY} (MPa)	S_{ZZ} (MPa)	E (MPa)
275 K (eq)	37.0	96.2	85.5	-0.1	-0.1	-0.1	N.A.
275 K (Y)	36.0	107.2	79.2	-0.1	10	-0.1	87
275 K (Z)	35.9	90.3	94.0	-0.1	-0.1	10	101
325 K (eq)	27.8	86.0	103.4	-0.1	-0.1	-0.1	N.A.
325 K (Y)	27.3	89.9	101.3	-0.1	10	-0.1	221
325 K (Z)	27.1	85.6	107.3	-0.1	-0.1	10	265

We did a quantitative comparison between the coarse-grained model and the experiment results. For instance, for the self-folding graphene flower, the average lateral size and height in the folded state measured by confocal microscopy was found to be 131 (±14) and 58 (±17) μm (Fig. 3C), and those values are 125 and 52 μm (Fig. 5C) in the simulation. For the graphene box, the size in the folded state is 326 μm, and in the simulation it is 340 μm. Those data demonstrate that the coarse-grained models are accurate representations of the experimental structures.

In addition, we also studied the effect of the overall size (or size/thickness ratio) on the self-folding behaviors. As shown in fig. S16, smaller flowers (120 and 300 μm) have more regular and well-defined folding morphology, while for larger ones (600 μm), the petals tend to twist or wrinkle during the folding process. The main reason is that for the large flowers, the initial folding direction can be either along the long axis, or in the middle between the long and short axis, and its initially curved structure increases the bending stiffness in the orthogonal direction and prevents folding in that direction. The interplay between initial folding direction and the energy release during the membrane bending determines the final folding structure.

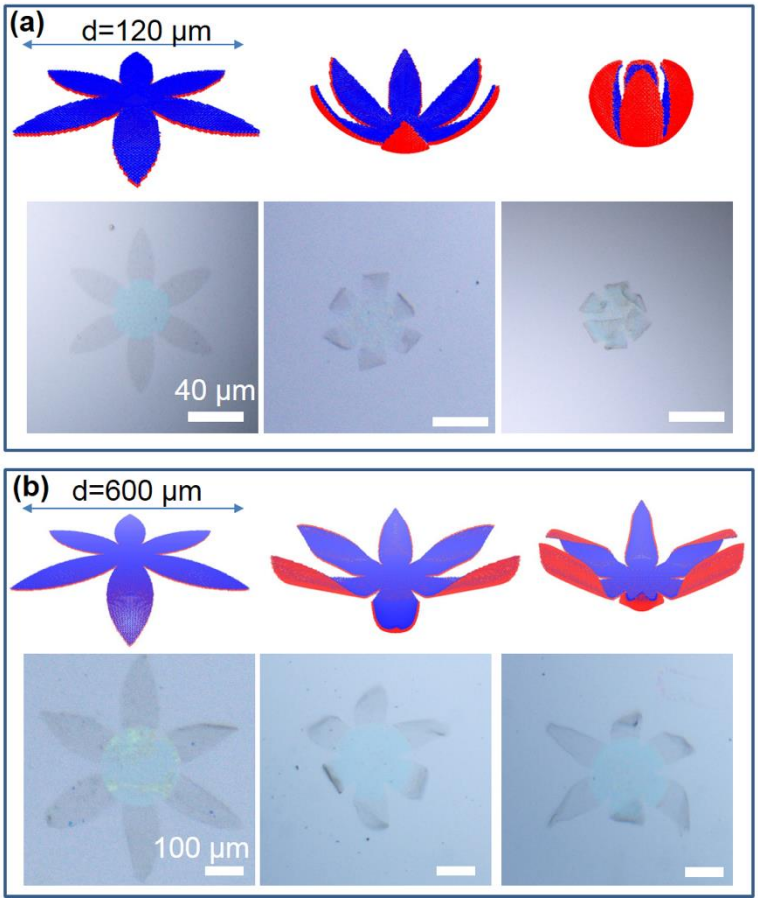

fig. S16. Comparison between the coarse-grained MD model and the experiment results for a functionalized graphene flower with different size. Panel (**a**) represents a flower with *d*=120 μm overall size of the initial pattern, and panel (**b**) is a *d*=600 μm flower.

Using this model, we can also design other material systems with different deforming ratio and material stiffness, which will play the main role in governing the resulting structure shape as shown in fig. S17. We can also change the fixed boundary condition and distribution pattern of the PNIPAM layer to result in different folded geometries.

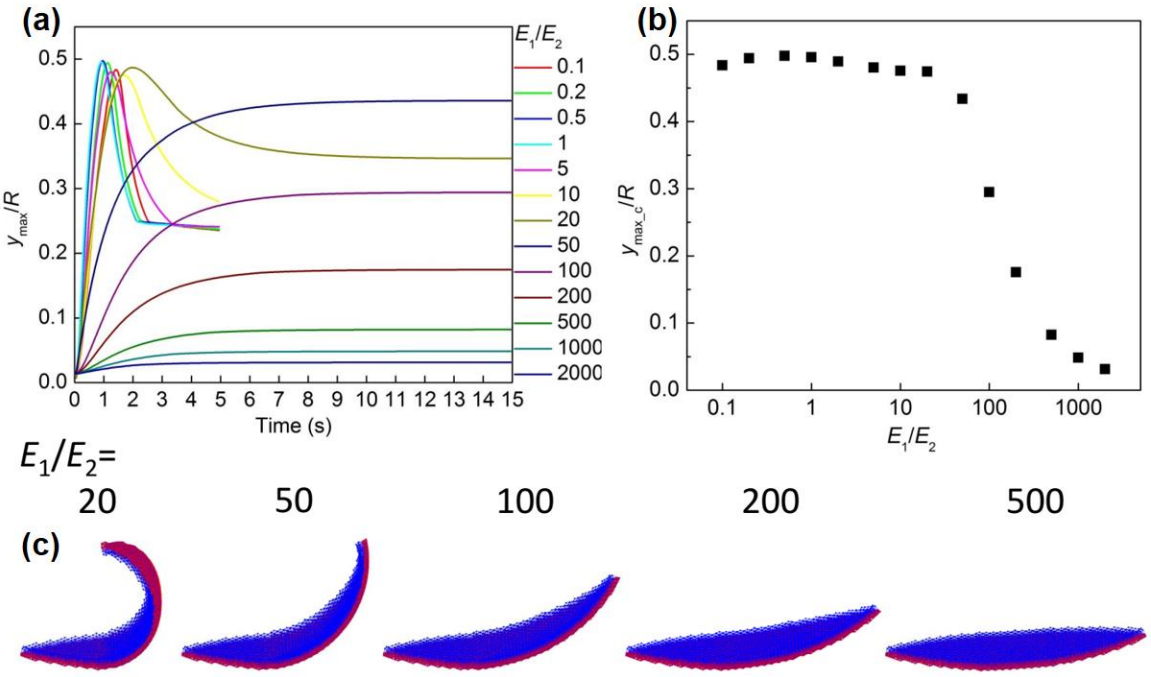

fig. S17. The effect of mechanical properties of the two layers on self-folding. The effect of the modulus ratio between the top (E_2) and bottom (E_1) layer on their folding behavior. (**a**) The maximum height (y_{max}) of the folded structure versus the overall radius (R) of the flower as a function of time. (**b**) The maximum height (y_{max_c}) of the folded structure versus the overall radius (R) of the flower as a function of the modulus ratio. (**c**) Simulation snapshots of the folded petals with different modulus ratio.

9. Electrical properties of folded graphene structures

The conductivity of the functionalized graphene microstructures was measured by the four-point probe method. The gold pads were placed directly on the graphene before it was functionalized with PD and PNIPAM. The functionalized graphene in the flat state has almost the same sheet resistance compared with that of pristine CVD graphene (fig. S18a).

As discussed in the main text, the folding crease can effectively alter the electrical property of functionalized graphene. In order to show that such a change is general and reproducible, we also conducted the same measurements on a graphene dumbbell with a different width of the folding crease, which is 20 μm, and other parameters are kept the same. The four-point probe measurement results are shown in fig. S18b, the general trend is the same with the dumbbell of 10 μm folding crease. The I-V curve becomes nonlinear after folding with a significant increase in resistance: 838 Ω before folding, and ranging from 1252 to1394 Ω after folding. The resistance of the folded dumbbell also has the maximum value around 0 V.

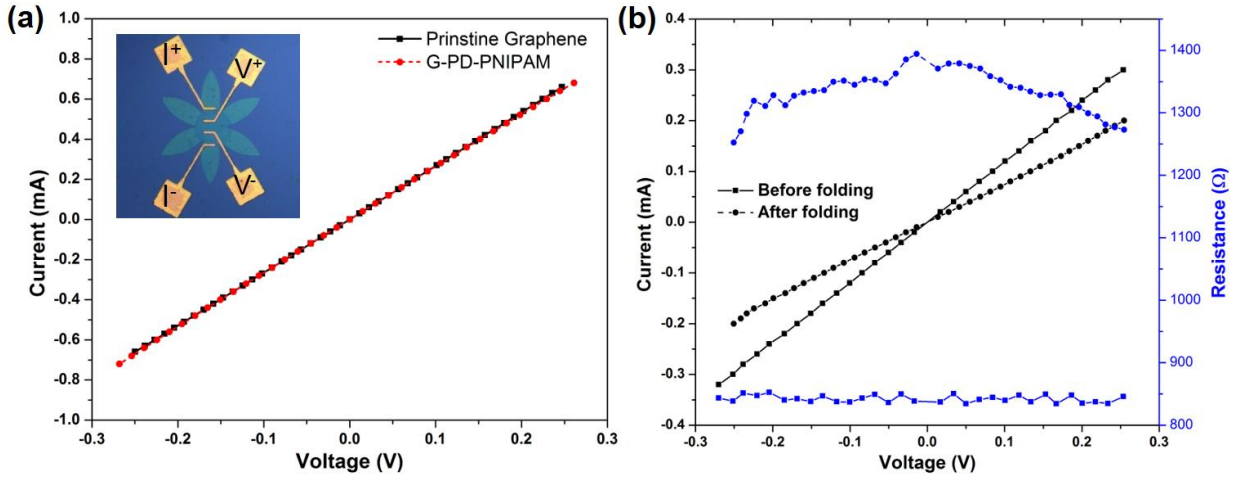

fig. S18. Electrical measurements on pristine graphene and functionalized graphene dumbbell. (**a**) I-V curves of the CVD graphene before and after surface functionalization, the inset is optical image of the 4-point probe device. (**b**) I-V curves and R-V curves of graphene dumbbell (with 20 μm wide center part) before and after folding.

The G-PD-PNIPAM has a total thickness of 8.9 nm in this study, so that when it folds on top of each other, a folding crease is formed at the edge, as shown in fig. S19. The SU-8 covered region is relatively far from the folding crease, so it does not have a significant effect on the crease formation. The height or diameter of the folding crease is measured by AFM, around 18 nm, which is quite small, but still much larger than that of a carbon nanotube, so that mechanical fracture of the graphene is unlikely to happen.

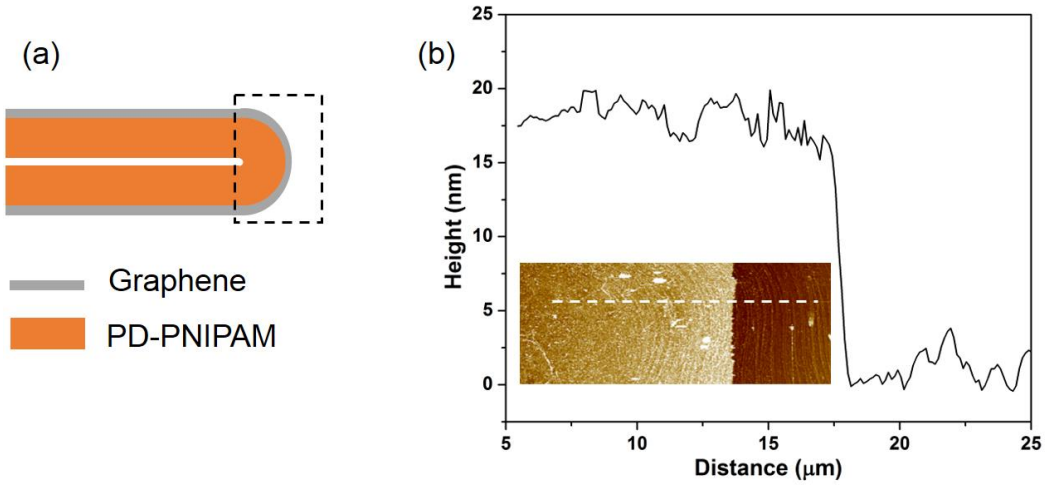

fig. S19. Dimension of the folding crease measured by AFM. (**a**) Schematic representation of the folding crease region, which is marked with a dash line box. (**b**) The height or diameter of the folding crease as measured by AFM cross-section analysis.

Figure S20a shows the output characteristics (I_d vs V_d) of the graphene FET on a 300 nm SiO_2 dielectric at different V_g (gate voltage). The channel width and length are 125 and 230 μm, respectively. The curve shows a perfect linear behavior and a decrease in conductance when the gate voltage changes from negative to positive values, which is typical for metal/graphene junctions. The transfer characteristics of the functionalized graphene FET is shown in fig. S20b. It can be seen that the Dirac current (I_d) gradually decreases with increasing V_g, and the Dirac point is approximately + 90 V, which indicates that the graphene is heavily p-doped, and the probable reason is the adsorption of water molecules from air and polymer residue from the transfer process. The output curves of the functionalized graphene FET are shown in fig. S20c. The behavior is similar to that of the pristine graphene FET, and proves that the non-covalent functionalization does not change the intrinsic electrical properties of graphene.

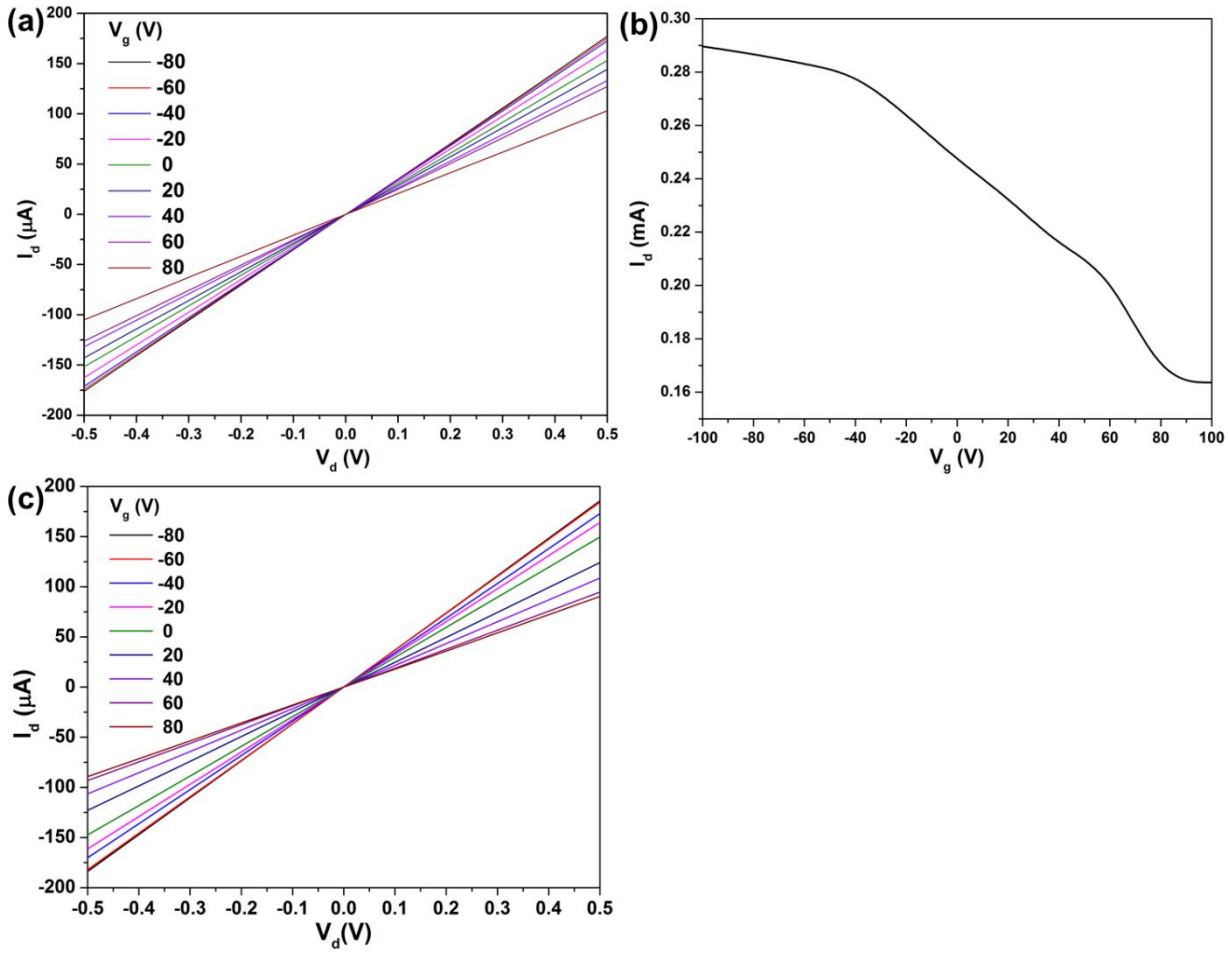

fig. S20. Output and transfer curves of the pristine and functionalized graphene FET. (**a**) Output curves of the pristine graphene FET as a function of bias with varying gate voltages. (**b**) Transfer curve of the pristine graphene FET as a function of back gate voltage. (**c**) Output curves of the functionalized graphene FET as a function of bias with varying gate voltages.